



Published in final edited form as:

Cell Rep. 2025 May 27; 44(5): 115591. doi:10.1016/j.celrep.2025.115591.

Simultaneous *in vivo* multi-organ fluxomics reveals divergent metabolic adaptations in liver, heart, and skeletal muscle during obesity

Mohsin Rahim^{1,3}, Tomasz K. Bednarski^{1,4}, Clinton M. Hasenour¹, Deveena R. Banerjee², Irina Trenary¹, Jamey D. Young^{1,2,5,*}

¹Department of Chemical and Biomolecular Engineering, Vanderbilt University, Nashville, TN, USA

²Department of Molecular Physiology and Biophysics, Vanderbilt University, Nashville, TN, USA

³Present address: Cytokinetics, Inc., South San Francisco, CA, USA

⁴Present address: Department of Nutrition and Health Sciences, University of Nebraska-Lincoln, Lincoln, NE, USA

⁵Lead contact

SUMMARY

We present an isotope-based metabolic flux analysis (MFA) approach to simultaneously quantify metabolic fluxes in the liver, heart, and skeletal muscle of individual mice. The platform was scaled to examine metabolic flux adaptations in age-matched cohorts of mice exhibiting varying levels of chronic obesity. We found that severe obesity increases hepatic gluconeogenesis and

This is an open access article under the CC BY-NC-ND license (<http://creativecommons.org/licenses/by-nc-nd/4.0/>).

*Correspondence: j.d.young@vanderbilt.edu.

AUTHOR CONTRIBUTIONS

Conceptualization, M.R., C.M.H., and J.D.Y.; methodology, M.R., C.M.H., and J.D.Y.; investigation, M.R., T.K.B., D.R.B., and I.T.; writing—original draft, M.R., C.M.H., and J.D.Y.; writing—review & editing, M.R., C.M.H., D.R.B., and J.D.Y.; funding acquisition, J.D.Y.; supervision, J.D.Y.

RESOURCE AVAILABILITY

Lead contact

Requests for further information and resources and reagents should be directed to and will be fulfilled by the lead contact, Jamey Young (j.d.young@vanderbilt.edu).

Materials availability

This study did not generate new unique reagents.

Data and code availability

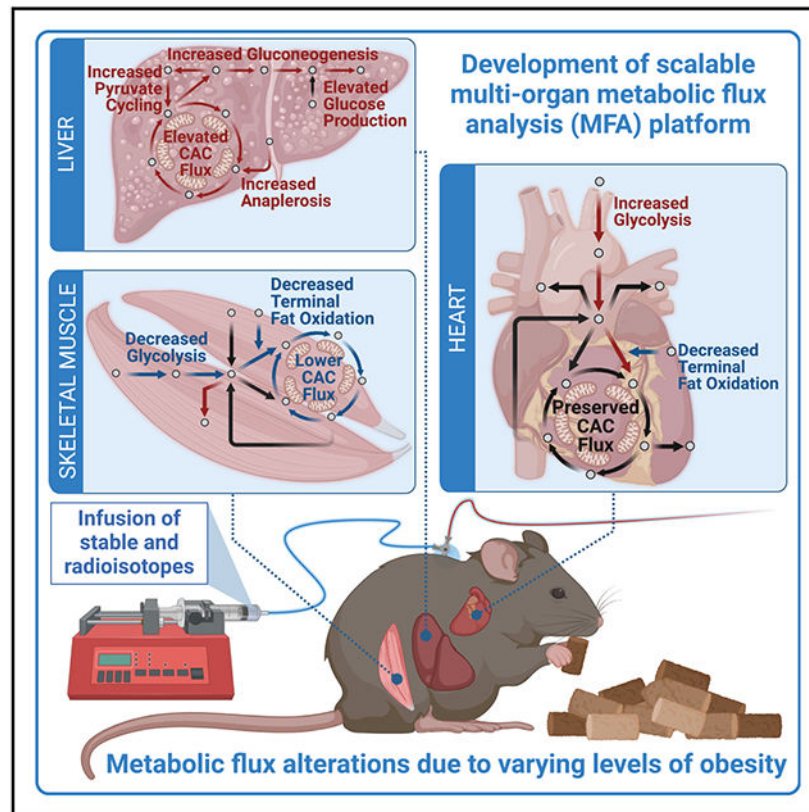
- Absolute flux measurements, tissue and plasma MIDs, metabolite concentrations, and mRNA fold changes have been deposited with Mendeley Data at <https://dx.doi.org/10.17632/dxc5yxysnm.1> and are publicly available as of the date of publication.
- Raw NanoString RCC files and metadata used for gene expression analysis are publicly accessible on the Gene Expression Omnibus (GEO: GSE291838).
- The INCA model is provided in Table S2 of the supplemental information.
- Any additional information required to reanalyze the data reported in this paper is available from the lead contact upon request.

DECLARATION OF INTERESTS

M.R. is currently an employee and shareholder of Cytokinetics. J.D.Y. is a cofounder of Metalytics.

citric acid cycle flux, accompanied by elevated glucose oxidation in the heart that compensates for impaired fatty acid oxidation. In contrast, skeletal muscle fluxes exhibit an overall reduction in substrate oxidation. These findings demonstrate the dichotomy in fuel utilization between cardiac and skeletal muscle during worsening metabolic disease and demonstrate the divergent effects of obesity on metabolic fluxes in different organs. This multi-tissue MFA technology can be extended to address important questions about *in vivo* regulation of metabolism and its dysregulation in disease, which cannot be fully answered through studies of single organs or isolated cells/tissues.

Graphical Abstract



In brief

Rahim et al. present a multi-tissue MFA platform to simultaneously quantify metabolic fluxes in the liver, heart, and skeletal muscle *in vivo*. They find that obesity causes divergent metabolic adaptations, including increased hepatic gluconeogenesis and a cardiac fuel shift toward glucose oxidation, while skeletal muscle reduced overall substrate oxidation.

INTRODUCTION

Metabolism is vital for cellular function: enzymes catabolize nutrients to generate chemical energy and intermediates that are then used to synthesize products required for cell growth and survival. A common approach for studying metabolism is through the measurement of gene, protein, and metabolite abundances of metabolic pathways. However, because

metabolic enzymes are tightly regulated by several factors such as allosteric feedback, post-translational modifications, and sub-strate/cofactor availability, static biomolecule abundances provide limited information about the flux of metabolites through a pathway.¹ In contrast, metabolic flux analysis (MFA) provides functional readouts of metabolic pathway activity, which is an ultimate representation of the cellular metabolic phenotype.²

The goal of preventing, diagnosing, and treating metabolic disease has led to the application of MFA in perfused tissues and *in vivo*.³ Assessment of *in vivo* metabolic fluxes has heavily focused on the liver, since it is a metabolic hub of the body and major site of obesity-induced disease pathogenesis. As a result, decades of work have generated refined *in vivo* methods for assessing gluconeogenesis, glycogenolysis, anaplerosis, citric acid cycle (CAC), lipid biosynthesis, fat oxidation, and ketogenesis fluxes in the liver.^{4,5} Though less prevalent than studies of the liver, metabolic fluxes have also been assessed in skeletal and cardiac muscle *in vivo*.⁶⁻⁹ By taking advantage of advances in computational and analytical technologies, some groups have recently quantified systemic fluxes of circulating metabolites, focusing on nutrient sources that serve as the primary fuel for specific tissues and the CAC.^{9,10}

Despite these pivotal advances, *in vivo* fluxomics faces the hurdle of more broadly contextualizing intermediary metabolic fluxes across tissues in the body's cross-regulatory homeostatic environment.¹¹ This limitation is particularly important for studies of pleiotropic disease states, pharmacological treatments, and genetic models that result in non-intuitive changes in physiology.¹² Here, we developed an isotopic flux modeling approach capable of simultaneously quantifying intermediary fluxes in both gluconeogenic and glycolytic tissues *in vivo*. We exploited the ¹³C labeling patterns generated by an infusion of [¹³C₃]lactate in fasted mice to quantify relative fluxes in the heart, gastrocnemius, vastus, and liver. Specifically, tissue-specific biochemistries were integrated into a mathematical model of *in vivo* physiology to determine fluxes from the stable-isotopic enrichment of metabolites throughout the body. The coinfusion of classical radiolabeled isotopes was used to convert relative fluxes to absolute rates.

This multi-tissue MFA framework was applied to identify metabolic dysfunction in multiple organ systems caused by hyperphagia and diet-related increases in adiposity and metabolic disease using the *Mc4r*^{-/-} mouse model. Mutations in the melanocortin-4 receptor (MC4R) are the most common monogenic cause of obesity in humans,¹³ and common *MC4R* variants are linked to polygenic obesity in the general population.¹⁴ Chow-fed *Mc4r*^{-/-} mice rapidly develop obesity and peripheral insulin resistance due to overt hyperphagia.¹⁵ When *Mc4r*^{-/-} mice are maintained on a Western diet (WD) that is high in saturated fat, cholesterol, and sucrose, they develop histological features of human steatohepatitis, including fibrosis and chronic inflammation.^{16,17} In addition, high-fat-fed *Mc4r*^{-/-} mice exhibit severe insulin resistance and reduced oxidative metabolism in skeletal muscle that is associated with increased adiposity relative to chow-fed animals.¹⁸ We therefore sought to examine the metabolic flux adaptations that occur under varying levels of obesity in chow-fed wild-type (WT), chow-fed *Mc4r*^{-/-}, and WD-fed *Mc4r*^{-/-} mice. The results demonstrate that mitochondrial metabolic fluxes were reduced in skeletal muscle but elevated in the liver of obese mice, while CAC flux in the heart was maintained via a switch in substrate preference from fat to glucose oxidation. Furthermore, flux alterations in heart and skeletal

muscle developed at a less severe stage of obesity compared to those in the liver. Overall, these results point to a divergence in the metabolic signatures of obesity in liver, heart, and skeletal muscle that could be leveraged for improved tissue-specific targeting of therapeutic interventions or diagnostic tests for treating the metabolic complications of obesity.

An integrated multi-tissue platform to assess metabolic flux *in vivo*

Years of research in metabolic modeling and isotope tracing served as building blocks of the multi-tissue model described here. In 2014, we introduced the first publicly available software package (INCA, Isotopomer Network Compartmental Analysis) capable of estimating metabolic fluxes based on either steady-state or dynamic isotope labeling measurements.¹⁹ Subsequently, INCA was applied to develop a novel microscale method to quantitatively assess hepatic glucose and CAC fluxes in unstressed mice.²⁰ This study was the first to estimate hepatic fluxes *in vivo* based on plasma samples obtained from a conscious mouse, and since then this methodology has been applied to a variety of mouse models during fasting^{16,21} and exercise.^{22,23} Recently, this single-compartment liver model was expanded to assess extrahepatic tracer recycling and Cori cycling²⁴ and to determine renal contributions to gluconeogenesis^{12,25} by adding a second compartment. The INCA software package was also adapted to model general combinations of mass spectrometry (MS) and magnetic resonance spectroscopy (MRS) isotopomer measurements.²⁶

Building on the previously published two-compartment models, which quantify *in vivo* flux alterations in gluconeogenic tissues of fasted mice, the current study aims to examine interactions between glucose-producing tissues (liver) and glycolytic tissues (heart and skeletal muscles) within a single mouse. Prior studies have used ¹³C-lactate infusions in mice²⁷ and human subjects²⁸ to establish that circulating lactate acts as a major carbon shuttle between numerous tissues in the body and may serve as the primary fuel for CAC metabolism in some tissues. Therefore, we extracted and analyzed metabolites from plasma, liver, heart, gastrocnemius, and vastus of conscious, unstressed mice infused with [¹³C₃]lactate. These mice were also infused with radioactive [3-³H]glucose, to assess endogenous glucose production rate (EndoRa), and with [1-¹⁴C]2-deoxyglucose (2-DG) to assess tissue-specific glucose uptake rate (R_g). Because of the negligible mass of radiotracers infused, the ³H and ¹⁴C enrichments can be used to determine absolute rates of EndoRa and extrahepatic R_g without interfering with stable isotope (¹³C) measurements. Fitting the ¹³C mass isotopomer distribution (MID) measurements from all tissues to an integrated multi-compartment metabolic model enabled relative fluxes to be estimated in liver and extrahepatic tissues, which were converted to absolute rates using radiotracer flux estimates (Figure 1). Gas chromatography-mass spectrometry (GC-MS) fragment ions used for determining fluxes in each compartment are listed in Table S1. Details of the model fitting procedure are described in the STAR Methods.

Multi-compartment model of whole-body and tissue-specific metabolism

The full metabolic network and carbon transitions used in the multi-compartment flux model are detailed in Table S2. The overall network can be decomposed into a “whole-body” outer model (comprising hepatic and extrahepatic compartments) and inner models that represent the tissue-specific metabolism of three extrahepatic subcompartments: heart, gastrocnemius,

and vastus. Metabolic equations were constructed from classical biochemical reactions and previously defined networks.^{20,24,29} The outer model is analogous to the model of Hasenour et al.,²⁴ while the inner models were constructed to reflect the central carbon and energy metabolism of each specific tissue type. Cardiac fluxes, including sources and sinks of carbon, were modeled based on prior findings.³⁰⁻³² Contributions of unlabeled carbon sources to glycolysis (e.g., glycogen) in the heart and skeletal muscle were modeled as a single flux, V_{PYGM} .^{8,33} Major carbon sinks for the heart and skeletal muscle were modeled as lactate, alanine, and glutamate, metabolites connected with anaerobic respiration and ammonia clearance. Unlabeled sources of acetyl-coenzyme A (CoA) may arise from multiple sources but, for parsimony, are modeled as a single flux ($V_{FatEntry}$) linked to β -oxidation. The model also included reactions that enable metabolic cross-communication between hepatic and extrahepatic compartments. Tissue-specific subnetworks for cardiac and skeletal muscle were modeled by allowing influx of source metabolites from the extrahepatic compartment and efflux of sink metabolites without altering the mass or isotopomer balances for the outer model or the adjacent subcompartment models (Figure 2A; Table S2).

This multi-compartment model has several unique aspects that extend beyond the biological applications presented here. First, the INCA software platform enables compartment-specific fluxes to be estimated individually for each mouse while integrating MID measurements from all tissues included in the metabolic network. This directly accounts for biological variability across animals and enables quantification of differences between tissues of individual mice. Moreover, robust statistical assessments, such as model goodness-of-fit tests and sensitivity analysis, are built-in features of INCA that facilitate the search for optimal flux solutions (see STAR Methods for further details). Second, the model was developed using a modular approach that enables seamless integration or removal of tissue-specific subnetworks without altering the description of other compartments. This adaptability allows researchers to further expand the metabolic model to include additional tissues or, conversely, simplify the model for more targeted studies. Third, the INCA modeling framework natively accounts for bidirectional isotopic exchange at metabolic nodes such as succinate dehydrogenase (SDH) and malate dehydrogenase (MDH) and can estimate reaction reversibility in the CAC by fitting the ^{13}C metabolite labeling data, as shown previously.²⁴ Last, and most importantly, the software platform is robust, adaptable, and freely available and automates the process of constructing and solving the model equations that describe any particular isotope labeling experiment. Therefore, researchers with biochemistry and physiology knowledge can analyze metabolic tracer data without the need to derive mathematical equations or write computer code required to rigorously solve systems of isotopomer balances.

RESULTS

Melanocortin-4 knockout mice exhibit diet-dependent changes in obesity and whole-body metabolism

To examine the effects of excess nutrient intake and diet composition on metabolism, lean mice (WT chow) were compared to hyperphagic *Mc4r* knockout (KO) mice placed on

chow (KO chow) or WD (KO WD). The body weight and fat mass of KO mice were elevated compared to WT mice, and both indices of obesity were further increased when KO mice were fed WD (Figures S1A-S1D). Impaired glucose tolerance (Figures S1E and S1F) and increased fasting plasma glucose and insulin levels (Figures S1G and S1H) were also observed in both KO cohorts, suggesting lower insulin sensitivity (i.e., higher homeostasis model assessment of insulin resistance [HOMA-IR] score) compared to WT controls (Figures S1I). To quantify metabolic fluxes, a mixture of stable and radioactive isotopes was infused into conscious, unrestrained mice via indwelling catheters implanted in the jugular vein and carotid artery. The rates of glucose turnover and, thus, endogenous glucose production (EndoRa) and disappearance (R_d) were significantly higher in the KO chow and KO WD groups (Figure S1J, note that $\text{EndoRa} = R_d$, since the mass of exogenous glucose infused was negligible). Consistent with increased whole-body R_d and elevated plasma insulin levels, tissue-specific glucose uptake (R_g) was increased in both cardiac and skeletal muscles of KO WD mice (Figures S1K-S1M). These data indicate stepwise increases in metabolic disease severity in KO chow and KO WD mice compared to WT chow mice.

Simultaneous flux assessment of liver, heart, and skeletal muscle reveals organ-specific metabolic signatures of obesity

To assess tissue-specific intermediary fluxes, metabolite MIDs were measured in plasma, liver, heart, gastrocnemius, and vastus tissues of mice following isotope infusions (Figure 1). Our previously developed two-compartment model of hepatic and extrahepatic metabolism²⁴ was expanded to include tissue-specific subnetworks for cardiac and skeletal muscles within the extrahepatic compartment (Figure 2A). Fitting the ¹³C labeling measurements in Table S1 to the multi-organ network outlined in Table S2 enabled simultaneous estimation of *in vivo* fluxes within each tissue. In addition to assessing metabolite abundances and flux, we measured mRNA expression of 72 hepatic genes (Figures 3I and S4), 60 cardiac genes (Figure S5), and 60 genes in gastrocnemius and vastus (Figures S6 and S7), all related to metabolism.

Consistent with previous reports,^{16,34} diet-induced obesity was associated with elevated fluxes in energy- and glucose-producing pathways of the liver. KO WD mice exhibited increased pyruvate cycling fluxes ($V_{\text{PEPCK,L}}$, $V_{\text{PK,L}}$, and $V_{\text{PC,L}}$) and a doubling of CAC activity (Figures 2B and 3D). Increases in CAC gene expression (*Cs* and *Idh2*) in KO mice directly correlated with elevated CAC flux (Figures 3I and S4). Expression of *Pklr* and *Pdk4*, genes encoding liver pyruvate kinase and pyruvate dehydrogenase kinase, corresponded with increased $V_{\text{PK,L}}$ and decreased $V_{\text{PDH,L}}$, respectively. In contrast, *Pck1* expression inversely correlated with phosphoenolpyruvate carboxykinase (PEPCK) flux, perhaps due to transcriptional feedback. Increased anaplerosis and cataplerosis through pyruvate carboxylase (PC) and PEPCK were associated with ~1.7- and ~1.5-fold increases in hepatic gluconeogenesis ($V_{\text{EnoL,L}}$) and endogenous glucose production (V_{EndoRa}), respectively (Figures 2B and 3D). Glycolytic fluxes in the extrahepatic compartment ($V_{\text{HK,E}}$ and $V_{\text{LDH,E}}$) also increased, indicative of elevated Cori cycling in KO WD mice. Similar flux trends were observed in KO chow mice, but the effects were less pronounced (Figures 3D and S2A).

The measured R_g in heart, gastrocnemius, and vastus (Figures S1K-S1M) was used to determine absolute fluxes within each extrahepatic subcompartment based on the relative flux solution derived from fitting the ^{13}C labeling data from each mouse. Similar to the liver, energy-producing fluxes were elevated in the heart tissue of KO WD mice (Figures 2C and 4A). Glycolytic fluxes were approximately doubled relative to WT controls (Figures 2C, 4A, and 4B). In contrast, CAC flux was reduced in KO chow mice, attributable to a decrease in acetyl-CoA entry from fatty acid oxidation (FAO) compared to WT controls (Figure S2B). WD feeding restored CAC activity in KO WD mice through an increase in glycolytic flux (Figure S2C). In contrast to myocardial metabolism, substrate oxidation was lower in skeletal muscle of KO WD mice despite a modest increase in muscle glucose uptake (Figures 2D and 2E). Both oxidative and anaerobic CAC fluxes were significantly reduced compared to controls, which decreased flux of pyruvate and acetyl-CoA into the CAC. These alterations in CAC activity were associated with reduced flux from glycogen into pyruvate and from fatty acids into acetyl-CoA, as well as less cataplerotic flux to pyruvate through malic enzyme. Similar perturbations in skeletal muscle metabolic fluxes were observed when comparing KO chow mice to WT controls (Figures S2D and S2E). These results demonstrate that flux adaptations in the skeletal muscle of obese mice diverged from those in the liver and heart, especially in mitochondrial oxidative and anaerobic pathways. Furthermore, similar levels of flux dysregulation were evident in the heart and skeletal muscle of both moderately obese (KO chow) and severely obese (KO WD) mice, whereas widespread flux dysregulation in the liver was observed only in KO WD mice.

Hepatic redox perturbations coincide with fatty liver disease progression

Elevated mitochondrial metabolism promotes oxidative stress and inflammation in livers of obese mice and humans.^{16,34,35} Therefore, we examined the impacts of obesity on markers of hepatocellular injury in the *Mc4r*^{-/-} mouse model. Histological analysis confirmed an increase in steatosis, fibrosis, hepatocellular ballooning, lobular inflammation, and elevated macrophage infiltration in livers of KO mice (Figures 3A, 3B, and S3A-S3D), which resulted in an overall elevation in nonalcoholic fatty liver disease (NAFLD) activity score that varied with extent of obesity (Figure 3C). Previous studies have shown that knockdown of liver PEPCK promotes a more reduced cytosolic and mitochondrial redox state and protects mice from hepatic oxidative stress and inflammation during high-fat feeding, whereas deletion of liver PC has the opposite effect on hepatic redox state and exacerbates diet-induced oxidative stress and inflammation.^{34,36} When analyzing liver metabolites from KO WD mice, we observed a 2-fold decrease in aspartate and malate and a 2-fold increase in pyruvate concentration relative to WT controls, which is indicative of a more oxidized cytosolic redox state (Figure 3E). Liver lactate/pyruvate and malate/pyruvate ratios (proxies of cytosolic NADH/NAD⁺ and NADPH/NADP⁺ ratios, respectively) confirmed that cytosolic redox state was significantly more oxidized in KO WD livers (Figure 3F and 3G). In contrast, mitochondrial redox state was more reduced in KO livers and varied with body weight (Figure 3H). Consistent with these findings, liver and plasma β -hydroxybutyrate levels were elevated (Figures S3F and S3G), indicative of elevated mitochondrial NADH/NAD⁺ ratio and increased ketogenesis. Higher mitochondrial NADH/NAD⁺ favors increased generation of reactive oxygen species, while lower cytosolic NADPH/NADP⁺ inhibits antioxidant functions,³⁷ both of which promote oxidative stress in liver. These redox

changes could also promote increases in hepatic gluconeogenesis and CAC fluxes observed in KO WD mice (Figure 3D).³⁸

Myocardial glucose oxidation is elevated, while fatty acid oxidation is reduced, in Western-diet-fed obese mice

Chow-fed KO mice exhibited a reduction in cardiac CAC flux ($V_{CS,H}$), primarily driven by a decrease in terminal FAO ($V_{FatEntry,H}$) (Figure 4A). When fed a WD, however, the reduction in fat oxidation was counterbalanced by a concurrent increase in pyruvate oxidation (Figure 4B), stemming from enhanced glucose uptake ($V_{HK,H}$) and glycogen breakdown ($V_{PYGM,H}$) in KO WD mice (Figure 4A). These findings demonstrate a shift in cardiac substrate utilization from fatty acids to glucose as obesity worsens, suggesting that elevated glucose oxidation may serve as a compensatory response to restore CAC flux (Figures 4A and 4B). Assessment of the cytosolic NADH/NAD⁺ ratio (Figure 4C) using cardiac lactate and pyruvate concentrations (Figure S5B) revealed a more reduced cytosolic redox state in KO mouse hearts, indicating increased glycolysis and/or decreased disposal of glycolytically produced NADH.³⁹ Elevated cardiac free fatty acid levels (Figure 4D) were consistent with the reduction in $V_{FatEntry,H}$. Expression of rate-limiting glycolytic enzymes *Hk2* and *Pfkfb1* was significantly upregulated, along with the gene encoding the muscle glucose transporter *Slc2a4* (Figures 4E and S5A). However, *Irs1* expression was downregulated (Figure 4F), possibly due to chronic hyperinsulinemia (Figure S1H).⁴⁰

Increased pyruvate dehydrogenase (PDH) flux ($V_{PDH,H}$) in KO WD mice corresponded with decreased *Pdk4* expression (Figures 4E and S5A), an inhibitor of PDH.⁴¹ Notably, the expression of *Crat*, a mitochondrial matrix enzyme that alleviates PDH feedback inhibition by removing excess acetyl-CoA,⁴² was upregulated in KO WD mice (Figure 4G). Gene expression of *Atp2a2* and *Ppara* was elevated, while *Ucp3* expression was reduced (Figure 4F), changes typically associated with increased mitochondrial energy production in the heart, consistent with elevated CAC flux in KO WD mice. Conversely, genes involved in mitochondrial biogenesis (*Nrf1* and *Tfam*) were slightly but significantly downregulated (Figure 4F). An upregulation in myocardial expression of genes involved in FAO (*Cpt1b*, *Cpt2*, *Acadm*, and *Acadl*) (Figure 4G), along with elevated cardiac, but not plasma (Figure S3H), free fatty acid levels and a significant decrease in $V_{FatEntry,H}$ flux, suggests impairments in cardiac FAO. This shift in substrate utilization from fatty acids to glucose aligns with the trade-off predicted by the Randle cycle. Notably, our results also indicate that impairments in FAO and the reduction in CAC flux observed in hearts of KO chow mice may precede elevations in glucose oxidation, which is possibly a compensatory mechanism to maintain ATP production for contractility.

Reduced skeletal muscle mitochondrial fluxes are indicative of defective substrate oxidation in obesity

Oxidative metabolic fluxes in both skeletal muscles gastrocnemius and vastus were significantly reduced in KO mice relative to WT controls (Figures 5A, 5B, 2D, and 2E). Glycolysis (VPK) and the expression of glycolytic genes (*Pygm*, *Pfkfb1*, and *Pkm*) were reduced in both tissues (Figures 5A-5D, S6A, and S7A). Consistent with these findings, the contribution of pyruvate to the CAC was significantly diminished in KO

mice compared to WT chow mice (Figures 5E and 5F). Acetyl-CoA entry into the CAC (VPDH and V_{FatEntry}) and anaplerosis from pyruvate (VPC) were significantly reduced in skeletal muscles of obese mice (Figures 5A and 5B). Contrasting with lower terminal fat oxidation flux (V_{FatEntry}), we measured an upregulation in the expression of genes connected with fat oxidation and carnitine production, suggesting potential compensation (Figures 5C, 5D, S6A, S6C, S7A, and S7C). Additionally, the branched-chain amino acid (BCAA) catabolic genes *Bcat1* and *Bcat2* were significantly downregulated in both skeletal muscles (Figures 5C and 5D) along with a rise in plasma BCAAs in KOWD mice (Figure S3I). Lower pyruvate anaplerosis through PC was associated with a reduction in the muscle lactate pool size (Figures 5G and 5H), which corresponded to a significantly more oxidized cytosolic redox state in both gastrocnemius and vastus of KO mice (Figures 5I and 5J). Gene expression of *Ldha* and *Ldhb* showed a decrease and an increase, respectively, in KO mice (Figures 5C and 5D), possibly to redirect pyruvate into mitochondria for complete oxidation.⁴³ These results demonstrate that obesity leads to a consistent reduction in glycolytic and mitochondrial fluxes in the skeletal muscle that results from perturbations in the metabolic pathways of glycolysis, FAO, and CAC anaplerosis.

Hyperphagia induces metabolic flux alterations similar to Western diet feeding

To disentangle the metabolic effects of hyperphagia-induced obesity and WD-induced obesity, WT mice fed a WD (WT WD) were compared to genetically obese KO chow mice. Despite similar weight gain (Figure S8A), WT WD mice had less lean mass (Figure S8B) and fat mass (Figure S8C), and they consumed less food (Figure S8D) due to the high calorie content of the WD. Interestingly, arterial glucose levels were consistent across groups (Figure S8E), but KO chow mice showed significantly elevated glucose turnover (R_d , which equals EndoRa) (Figure S8F), indicating increased hepatic gluconeogenesis. Both KO chow and WT WD mice exhibited clear signs of insulin resistance, as reflected by intraperitoneal glucose tolerance tests (Figures S8G and S8H), fasting plasma insulin levels (Figure S8I), and HOMA-IR scores (Figure S8J), with KO chow mice demonstrating more severe insulin resistance than WT WD mice. Cardiac glucose uptake fluxes were unchanged between WT WD and KO chow mice (Figure S8K), whereas skeletal muscle glucose uptake was increased in KO chow mice (Figure S8L and S8M), possibly in response to elevated plasma insulin and EndoRa levels.

Both hyperphagia-induced and WD-induced obesity resulted in similar metabolic flux alterations across tissues. KO chow mice displayed significant increases in hepatic gluconeogenesis (V_{Enol}), endogenous glucose production (EndoRa), and citrate synthase (V_{CS}) flux compared to WT chow mice, whereas these differences did not achieve significance in WT WD mice (Figure 6A). Both KO chow and WTWD mice exhibited elevated pyruvate cycling, but KO chow mice uniquely had higher PDH (VPDH) and lactate dehydrogenase (LDH) (VLDH) fluxes, reflecting enhanced pyruvate metabolism in the context of hyperphagia (Figure 6A). Despite these distinct differences between WT WD and KO chow mice, we observed some common patterns of hepatic flux dysregulation when compared to lean WT chow mice, suggesting a partial convergence of liver metabolic phenotypes in hyperphagia- and diet-induced obesity. This convergence was also evident in histological markers of non-alcoholic steatohepatitis (NASH), where hepatic steatosis,

hepatocellular ballooning, inflammation, NALFD activity score, and macrophage infiltration were similarly elevated in both WT WD and KO chow groups (Figures S8P-S8T). However, it's important to note that this convergence is not complete, and significant differences remain between the WT WD and the KO chow mice. For example, livers of WT WD mice had more macrovesicular steatosis and fibrosis compared to KO chow mice (Figures S8N and S8O).

In the heart, no significant differences were found between fluxes of KO chow and WT WD mice, suggesting that both obesity models similarly alter cardiac metabolism (Figure 6B). However, the reductions in FAO and CAC flux observed in KO chow mice did not achieve significance in WT WD mice. In skeletal muscle, both the gastrocnemius and the vastus muscles showed reduced glycolytic (V_{PK}) and mitochondrial (V_{CS}) fluxes in KO chow and WT WD mice compared to WT chow mice, primarily due to decreased glycogen utilization (Figures 6C and 6D). FAO in the gastrocnemius was significantly lower in WTWD mice compared to WT chow, with a similar trend in KO chow mice (Figure 6C). In contrast, glucose uptake in the vastus was elevated in KO chow mice compared to both WT WD and WT chow mice, though glycolytic flux remained suppressed due to reduced glycogen breakdown (VPYGM) (Figure 6D). These results indicate that, despite diet-specific metabolic differences, both models of moderate obesity produce similar signatures of metabolic flux dysregulation.

DISCUSSION

Prior studies have applied isotope tracers to investigate the effects of obesity and high-fat diets on metabolic fluxes within specific tissues.^{16,34,44} To our knowledge, no studies have introduced stable isotope methods that simultaneously assess intermediary metabolic fluxes within and between different gluconeogenic and glycolytic tissues in a single mouse. Here, a mathematical modeling approach was developed to quantify metabolic fluxes in multiple tissues with the generalizability and scalability to test hypotheses under a wide range of physiological conditions. We applied this novel ^{13}C MFA platform to examine the impact of hyperphagia and WD feeding on hepatic, cardiac, and skeletal muscle fluxes in a genetically obese mouse model that exhibits several representative features of human metabolic disease. Similar to previous findings, CAC fluxes, pyruvate cycling, gluconeogenesis, and endogenous glucose production were elevated in the livers of obese mice. These flux alterations were associated with divergent changes in cytosolic and mitochondrial redox states, which are hypothesized to promote oxidative stress and insulin resistance. While overconsumption of a normal chow diet decreased CAC flux in hearts of KO mice, WD-fed KO mice preserved cardiac energy metabolism by switching the major mitochondrial fuel source from fat to glucose (Figure 7). In contrast, glycolytic and mitochondrial oxidative fluxes were substantially lower in skeletal muscles of KO mice, despite an increase in glucose uptake, and the changes were fully developed even at moderate levels of obesity in both WT WD and KO chow groups. These findings illustrate distinct metabolic flux signatures within each organ that develop along different stage-dependent trajectories as the severity of metabolic disease progresses.

Alterations in glycolytic and mitochondrial metabolism can cause redox imbalance, which contributes to the development of metabolic syndrome and insulin resistance.⁴⁵ For example, higher mitochondrial NADH/NAD⁺ ratios estimated in the livers of KO WD mice are also associated with steatosis, hepatocellular ballooning, lobular inflammation, NAFLD activity score, and fibrosis in humans independent of age, sex, BMI, and diabetes.⁴⁶ Similarly, high-fat feeding has been shown to reduce glycolysis⁴⁷ and lower fat oxidation in skeletal muscle.⁴⁸ These findings are consistent with our results, which indicate that glycolysis and CAC flux were decreased in skeletal muscle of obese mice, potentially explaining the shift toward a more oxidized cytosolic redox state. Conversely, glycolytic and CAC fluxes were increased in hearts of KO WD mice, concomitant with a shift toward a more reduced cytosolic redox state. Therefore, the tissue-specific cytosolic and mitochondrial redox perturbations reported here may be a consequence of the metabolic flux alterations observed in each organ, which underlie their different pathways of metabolic disease progression (Figure 7).

The metabolic response of cardiac and skeletal muscle to obesity has previously been examined and is indicative of varying insulin sensitivity of the different tissues.⁴⁹ Patients with type 1 or type 2 diabetes—but no history of coronary heart disease—exhibited signs of insulin resistance in the skeletal muscle but had no alterations in myocardial glucose uptake under insulin-stimulated conditions.⁴⁹⁻⁵¹ Nevertheless, reduced cardiac glucose uptake and increased FAO are hypothesized causes of cardiac dysfunction in animal models of obesity and insulin resistance.^{52,53} This hypothesis stems largely from work performed in isolated hearts or cultured cardiomyocytes with glucose and palmitate as the sole substrates.⁵⁴ The complexity of *in vivo* pathophysiology suggests a more nuanced relationship between substrate availability and utilization, however. We observed that 8 weeks of WD feeding increased flux of acetyl-CoA into the CAC from glucose ($V_{PDH,H}$) but decreased flux from non-glucose sources ($V_{FatEntry,H}$) in hearts of KO mice, with net preservation of CAC flux ($V_{CS,H}$) to meet the cardiac energy demands of obesity (Figure 4). These results are consistent with other *in vivo* studies conducted using [¹⁸F]2-fluoro-2-deoxy-D-glucose and PET imaging that indicate glucose uptake is markedly elevated in the hearts of both young and middle-aged mice fed a high-fat, high-cholesterol WD.⁵⁵ Moreover, the development of pressure-overload-induced cardiac hypertrophy has been linked to concurrent increases in glycolysis and decreases in FAO,^{56,57} similar to our findings. Discrepancies between the results reported here and elsewhere likely stem from the hyperinsulinemic and hyperglycemic state of KO WD mice compared to lean control mice (Figure S1), as well as other challenges associated with replicating the *in vivo* milieu of the obese heart using an *in vitro* or perfusion system.

Previous *in vivo* ¹³C MRS studies performed in lean, insulin-resistant human subjects and high-fat-fed rats indicate that reductions in mitochondrial function are associated with intramyocellular lipid accumulation and muscle insulin resistance.^{6,58} However, discrepant results have been obtained from other studies of rat skeletal muscle showing that mitochondrial oxidative capacity is unchanged⁵⁹ or even increased⁶⁰ in obesity. The results here show a significant decrease in glycolytic and CAC flux in the skeletal muscle of obese mice during fasting (Figures 5A and 5B). The decreased glycolytic flux was due to reduced glycogen breakdown rather than diminished glucose uptake, which could be

connected with an impairment in glycogen synthase observed in obese, insulin-resistant humans.^{61,62} Our transcriptomics results showed a significant upregulation in FAO genes, suggesting elevated β -oxidation in the skeletal muscles of obese mice (Figures 5C and 5D). Despite elevated FAO gene expression, acetyl-CoA production from both fat oxidation and PDH was decreased (Figures 5A and 5B), with the latter known to be potently inhibited by fatty acids.⁶³ These results are consistent with previous findings that high-fat feeding increases incomplete FAO in the skeletal muscle unmatched by compensatory increases in CAC activity in both animals and humans.⁶⁴⁻⁶⁶ Furthermore, our results provide support for the concept of “metabolic inflexibility” of skeletal muscle in obese individuals, whereby insulin resistance is linked to a blunted mitochondrial capacity to effectively switch from glucose to fat oxidation during the transition from a fed to a fasted state.⁶⁷

Our study demonstrates that the vastus and gastrocnemius muscles exhibit similar shifts in metabolic flux as a result of obesity (Figures 5A-5D). Both muscles are predominantly composed of type II (fast-twitch) fibers and share a comparable distribution of fiber types, with gastrocnemius being somewhat higher in type I (slow-twitch) fibers in human samples but not in samples from rodents and other mammals.⁶⁸ Comparative analyses have shown a similar enzymatic profile between these muscles, except for LDH, which is expressed at significantly higher levels in the vastus.⁶⁸ This aligns with our findings, where elevated LDH flux was observed in the vastus relative to the gastrocnemius across all three groups. Previous studies have also shown that increased adiposity and obesity are associated with a reduction in type I fibers in the vastus and gastrocnemius,^{69,70} which typically have a higher oxidative capacity for both glucose and fatty acids.⁷¹ The overall reduction in glucose oxidation and CAC flux due to obesity may therefore reflect shifts in skeletal muscle fiber composition and muscle mass.

Our study also elucidates the subtle differences in physiology between two models of moderate obesity caused by overt hyperphagia (KO chow mice) vs. WD feeding (WT WD mice). While fat mass, plasma insulin levels, glucose turnover rate, and HOMA-IR differentiate the two groups (Figures S8A-S8J), metabolic flux alterations within tissues of WT WD and KO chow mice exhibited similar overall trends (Figure 6). Compared to lean (WT chow) mice, flux changes were more pronounced in skeletal muscle than in the liver or heart of WT WD and KO chow mice. Consistent with these data (Figure 6A), prior studies have demonstrated progressive hyperactivation of hepatic fluxes during an extended time course of WD feeding, with pyruvate cycling fluxes typically dysregulated prior to other mitochondrial and glucose-producing fluxes.^{24,72} Moreover, approximately 8 weeks of WD feeding in C57BL/6 mice had minimal impacts on cardiac function indicators, such as ejection fraction and fractional shortening,⁷³ aligning with the limited effects on cardiac metabolism we observed in WT WD and KO chow groups compared to WT chow (Figure 6B). Similarly, previous studies report that both hyperphagia⁷⁴ and WD feeding⁷⁵ reduce the expression of glucose and oxidative metabolism genes in skeletal muscle, consistent with our gene expression data and aligning with our metabolic flux findings. Collectively, these results suggest that moderate obesity induced by either hyperphagia or 8 weeks of WD feeding elicits similar disruptions in metabolic flux across multiple tissues, which become more widespread and further amplified in the severely obese KO WD model.

Advancements in analytical platforms and mathematical modeling have enabled *in vivo* flux analysis to become an important tool for studying physiology and metabolic diseases.^{5,10,27,76} In general, previous studies have prioritized studying intermediary metabolic activity of individual tissues, which likely results from balancing practical constraints with research interests. The flexible platform presented here was designed to enable researchers to maximize the flux information available in a single *in vivo* isotopic labeling experiment and broadly capture changes in metabolism across multiple tissues. Specifically, the technology allows either a focused or a comprehensive assessment of intermediary metabolic fluxes in different organ systems and, to demonstrate its utility, was applied to examine the response to stage-wise increases in obesity as a relevant metabolic stressor. Metabolic models were constructed with software that eliminates the tedium and potential mistakes of manually generating and solving the mathematical equations required for flux analysis. By reducing the time spent adding, removing, modifying, and solving equations, researchers can focus on building models and performing experiments to test new hypotheses. We expect that the generality and flexibility of this platform will facilitate the use of multi-organ fluxomics to examine a variety of important questions in metabolism research.

In summary, we present the development and application of a novel multi-tissue MFA platform that can be applied to simultaneously assess intermediary metabolism in the liver, heart, and skeletal muscle of individual mice based on isotope enrichment measurements of tissue and plasma metabolites. By making use of technical and computational advancements in systems biology, our study shows that isotopic tracing and rigorous data modeling can quantify *in vivo* metabolic fluxes that are otherwise unobservable. Applying the multi-tissue model developed herein, we demonstrate the broad impact of obesity on specific organs, reinforcing the notion that metabolic disease is unlikely to manifest in the same manner or to a similar extent in different organs within a single individual. Overall, the development of this *in vivo* ¹³C MFA approach provides a flexible analytical platform that can be applied to investigate the metabolic response to many other genetic, physiological, or pharmacological interventions that simultaneously impact multiple organ systems and can be expanded to include other metabolic tissues of interest.

Limitations of the study

The multi-compartment model applied here relies upon assumptions with inherent limitations. The model does not account for additional sources of glucose synthesis other than the liver. However, the scalability of this flux approach allows for the addition of other gluconeogenic or glycolytic tissues if required. The model aggregates all non-pyruvate sources of acetyl-CoA into a single flux (V_{FatEntry}), which represents terminal FAO but may also include contributions from other mitochondrial fuel sources such as BCAAs or ketone bodies. Existing literature indicates that the contribution of BCAAs to the mitochondrial acetyl-CoA pool is minimal, accounting for less than 10% of the total.⁹ However, resolving specific fluxes involved in the metabolism of fatty acids, ketone bodies, or BCAAs—or whole-body turnover of these substrates—would require a different set of tracers and metabolite measurements. Furthermore, the NanoString panel was specifically designed to assess gene expression within pathways included in the flux model, and

so coverage of auxiliary pathways (e.g., BCAA catabolism) is limited. The glycolytic metabolic model for the heart and skeletal muscle does not include the oxidative pentose phosphate pathway (oxPPP) due to lack of enrichment measurements of sugar phosphate intermediates. Although oxPPP activity is considered to be low in cardiac⁷⁷ and skeletal muscles,⁷⁸ future studies benefiting from the use of liquid chromatography-tandem mass spectrometry (LC-MS/MS) measurements could further explore metabolic fluxes within this pathway.⁷⁹

There are also potential limitations due to the study design. First, the choice of experimental model will influence the results. Mice were fasted overnight prior to the start of the isotope infusion, and the results should be interpreted only within this defined metabolic context. This condition was chosen to maximize ¹³C enrichment due to infusion of the lactate tracer, minimize variability due to differences in nocturnal feeding patterns, and maintain consistency with previous liver-specific flux analyses reported by our group²⁴ and others.^{80,81} Although *Mc4r*^{-/-} mice are commonly used for studying hepatic steatosis and obesity, this model develops dilated cardiomyopathy at ages older than those studied here.⁸² When studying multiple tissues simultaneously, the choice of any obese mouse model will have inherent limitations that need to be recognized. It should also be noted that the mice included in this study were all male, but application of the same flux analysis workflow to female mice would enable investigations of sex-specific differences in the pathogenesis of obesity and cardiometabolic diseases. Second, we did not independently confirm steady-state labeling in tissues. A unique facet of our experimental system is the ability to measure plasma glucose enrichment over time and verify steady-state labeling during the isotope infusion time course, which we have confirmed previously for a 2-h infusion of ¹³C-propionate.²⁰ Other groups have confirmed isotopic steady-state in tissue metabolites after 2.5 h of ¹³C-glucose infusion²⁷ or 1.5 h of ¹³C-glutamine infusion⁸⁰ using separate cohorts of mice sacrificed at different time points. Based on the high turnover rate of circulating lactate in fasted mice,²⁷ we expect that isotopic steady state is achieved with ¹³C-lactate more rapidly than ¹³C-propionate, ¹³C-glucose, or ¹³C-glutamine tracers. However, endpoint measurements of tissue metabolites can be obtained only in a terminal sample and, therefore, steady-state assumptions for tissue metabolites cannot be independently confirmed in each animal. In light of this fact, the 2-DG bolus was administered at a minimal dose to avoid significant metabolic perturbations, following methods described previously.⁸³ Mice were surgically equipped with carotid artery and jugular vein catheters to limit mouse handling stress during isotope infusions and blood sampling.^{84,85} Cervical dislocation was used for euthanasia to exclude the potential impact of anesthetics⁸⁶ on our measurement set and because of its common use in other *in vivo* metabolic tracer experiments.^{8,27,87} However, we cannot exclude the possibility that euthanasia method and tissue collection procedures influenced the outcomes presented here, as well as those in other studies using similar techniques, given that all measurements (not just metabolic fluxes) can be influenced by these methodological choices.⁸⁸⁻⁹⁰ Tissues were rapidly collected in a consistent order and flash frozen to minimize sampling artifacts, but, nevertheless, a study to evaluate the potential impact of euthanasia and tissue collection on *in vivo* isotope labeling patterns would be an informative addition to the field.

STAR★METHODS

EXPERIMENTAL MODEL AND STUDY PARTICIPANT DETAILS

All protocols and procedures were approved by the Vanderbilt Institutional Animal Care and Use Committee. All studies were performed on ~16-week-old, male hyperphagic *Mc4r^{-/-}* mice (knockout, KO) or wild-type (WT) littermates on a C57Bl/6J background; breeders were generously provided by the Roger D. Cone laboratory.⁹¹ Mice were maintained on a 12-h light-dark cycle with *ad libitum* access to water and a standard rodent chow diet (5L0D, 29% protein, 58% carbohydrates, 13% fat by caloric contribution; LabDiet, St. Louis, MO) for 8 weeks. At 8 weeks of age, half of the WT and KO mice were switched to a Western-style diet (D12079B, 17% protein, 43% carbohydrates, and 40% fat by caloric contribution; Research Diets Inc., New Brunswick, NJ) while others were kept on chow diet for another 8 weeks. Overall, four groups were utilized for these studies: chow-fed WT mice (WT Chow), chow-fed KO mice (KO Chow), WT mice fed a Western diet (WD) for 8 weeks (WT WD), and KO mice fed WD for 8 weeks (KO WD).

METHOD DETAILS

***In vivo* procedures in the conscious mouse:** One week prior to studies, jugular vein and carotid artery catheters were surgically implanted in 15-week-old mice for venous infusions and arterial blood sampling, respectively.⁸⁴ A combination of stable and radioactive isotope tracers was administered to overnight-fasted (~16h) mice over a total time course of 180min. Throughout each study, blood glucose levels were monitored using an Accu-Check glucometer (Roche Diagnostics, Indianapolis, IN), and hematocrit was maintained through an infusion of donor erythrocytes (suspended in 10U/mL heparinized-saline). Mice received a primed (1.5 μ Ci), continuous (0.075 μ Ci/min) infusion of [3-³H] glucose starting at t=0min. Then, a primed (0.200 mmol/kg), continuous (0.050 mmol/kg/min) infusion of [¹³C₃]lactate was administered starting at t=60min. Lastly, a 12 μ Ci bolus of [1-¹⁴C]2-deoxyglucose (2-DG) was introduced at t=155min. Blood samples were collected just prior to [¹³C₃]lactate infusion, and then at 2, 5, 10, 15, and 25min after the [¹⁴C]2-DG bolus. Following the final blood sample, mice were euthanized via cervical dislocation, and excised tissues were snap frozen in liquid nitrogen and stored at -80°C. Tissues were rapidly collected in a consistent order of liver, skeletal muscle, and heart, and immediately frozen in liquid nitrogen to mitigate potential effects of post-mortem metabolism on isotopic measurements.

Liver histology, plasma analysis, and body composition measurements:

Additional age-matched mice from each group were maintained similarly—except without surgery or isotope infusions—for body composition, blood biochemistry, tissue histology, and gene expression analysis following an overnight fast (~19h). Body composition was assessed using a Bruker Minispec benchtop pulsed NMR (7T) system (model mq7.5, Bruker, Billerica, MA). Mice were placed in a restrainer to obtain plasma (isolated from blood collected from the cut tail), and tissues were rapidly collected and snap frozen in liquid nitrogen post euthanasia. Plasma glucose concentrations were determined using an Accu-Chek glucometer. Insulin was measured with radioimmunoassay RI-13K (MilliporeSigma, Burlington, MA). Liver histology was assessed as previously described¹⁶. Briefly, liver

tissues were fixed in formalin, embedded in paraffin, and cut into sections. Hematoxylin and eosin (H&E) stained sections of liver from each mouse were evaluated for evidence of nonalcoholic steatohepatitis (NASH) markers by a board-certified veterinary pathologist in blinded fashion. Scoring was based on previously published criteria.⁹²

Metabolite extraction, derivatization, and GC-MS analysis: Plasma and tissue metabolites were extracted and derivatized as described elsewhere.²⁴ Briefly, plasma aliquots used for analysis of glucose labeling were extracted with cold acetone to precipitate protein. Samples were air-dried and immediately processed to convert glucose to its di-*O*-isopropylidene, methyloxime pentapropionate, or aldonitrile pentapropionate derivative according to protocols described elsewhere (Antoniewicz et al., 2011). Polar metabolites were isolated from 40 μ L of plasma or 30-50 mg of liver, heart, gastrocnemius, and vastus tissues using a biphasic methanol/water/chloroform extraction. The polar layer of the extract was isolated using a fine-tipped pipette and air-dried overnight for storage at -80°C prior to derivatization. Ten μ L of 5-mM norvaline was spiked as an internal standard for metabolite quantification. Metabolites were then converted to their methyloxime *tert*-butyldimethylsilyl (Mox-TBDMS) derivatives using methoxyamine hydrogen chloride (ThermoFisher Scientific) and MtBSTFA+1% TBDMCS (Regis Technologies). Derivatized samples were analyzed by GC-MS. Sample volumes of 1 μ L were injected using a 5:1 split on an Agilent 7890A gas chromatography system equipped with two HP-5ms (15 m x 0.25 mm x 0.25 mm; Agilent J&W Scientific) capillary columns in series and interfaced with an Agilent 5977C mass spectrometer. Helium was used as carrier gas, maintained at a constant flow rate of 1 mL/min throughout the analysis. The inlet temperature was set to 270°C , while the interface temperature was maintained at 300°C to ensure efficient transfer of the analytes into the mass spectrometer. The temperature program began with an initial hold at 80°C for 2 minutes. The temperature was then increased at a rate of 20°C per minute until reaching 140°C , followed by a slower ramp of 4°C per minute until 280°C was achieved. This final temperature was held constant for 5 minutes, resulting in an overall run time of approximately 45 minutes. The mass spectrometer was operated in scan mode, with data collected over an *m/z* range of 100 to 550. A solvent delay of 5 minutes was implemented to prevent solvent-related interference during the early stages of the analysis. The GC-MS settings described here are similar to previously published parameters for Mox-TBDMS⁹³ and glucose derivatives²⁰. Derivative peaks were integrated using the PIRAMID package⁹⁴ to obtain mass isotopomer distributions (MIDs) for the metabolite fragment ions shown in Table S1. Measurement uncertainty was assessed by calculating the root-mean-square deviation between the MID of unlabeled standards and the theoretical MID computed from the known abundances of naturally occurring isotopes.

Multi-tissue metabolic flux analysis (MFA): MFA was performed by minimizing the sum of squared residuals (SSR) between model-simulated and experimentally measured metabolite MIDs. The Isotopomer Network Compartmental Analysis (INCA) software package¹⁹ was used to develop metabolic models and determine all fluxes by least-squares regression. Plasma, liver, heart, gastrocnemius, and vastus metabolite MIDs were provided as measurements to INCA. The uncertainty in these measurements was set to either the root-mean square error of unenriched control samples or the SEM of technical GC-MS

replicates, whichever was greater. Best-fit flux solutions were determined for each animal by fitting experimental measurements to the isotopomer network model. To ensure a global solution was obtained, flux estimations were repeated a minimum of 100 times from randomized initial guesses. A chi-square test was used to assess goodness-of-fit, and sensitivity analysis was performed to determine 95% confidence intervals associated with the calculated flux values. All model fits were accepted with average SSRs (\pm SEM) of 179.6 ± 12.5 for WT Chow (n=8), 118.7 ± 2.8 for WT WD (n=6), 197.9 ± 8.6 for KO Chow (n=7), and 171.8 ± 12.3 for KO WD (n=6), which were below the upper 95% confidence limit of 325. Initially, fluxes in the hepatic and extrahepatic compartments were estimated relative to liver citrate synthase flux by constraining VCS.L to an arbitrary value of 100. Relative cardiac and skeletal muscle fluxes were estimated by setting the glucose uptake flux (VHK) to 100 in those subnetworks. Endogenous glucose production (VEndoRa) and the rate of glucose disappearance (R_d) were determined using Steele's steady-state equations, assuming $R_d = \text{EndoRa}^{95}$; V_{EndoRa} was used to convert relative hepatic and extrahepatic fluxes to absolute rates. Similarly, relative cardiac and skeletal muscle fluxes were converted into absolute rates using R_g , an index of tissue-specific glucose uptake, determined from [^{14}C]2-DG administration⁹⁶.

Gene expression analysis: RNA was isolated from ~30 mg of liver, heart, gastrocnemius, and vastus using Trizol reagent (Invitrogen), according to manufacturer protocols. To eliminate phenolic impurities carried over from the Trizol extraction, we further processed the samples using a RNeasy mini kit (Qiagen, Hilden, Germany). RNA yield from each sample was determined using a NanoDrop ND-100 spectrophotometer (Thermo Scientific, Wilmington, DE), and RNA integrity was determined using a 2100 Bioanalyzer (Agilent Technologies, Santa Clara, CA). RNA transcript abundance for each tissue was analyzed using the NanoString nCounter mRNA custom codeset panel, according to manufacturer protocols. Briefly, hybridization reactions were set up by adding 10 μL of hybridization buffer, 5 μL of TagSet Master mix, 5 μL of Extension TagSet, 1 μL of 30x working probe A pool, 1 μL of 30x working probe B pool, 3 μL of DNase/RNase free water and 5 μL of RNA Sample (20 ng/ μL), for a total volume of 30 μL to each sample tube. The samples were hybridized at 67°C for 16 hours. The hybridized samples were then analyzed using the FLEX system's nCounter Prep Station, and the cartridge was scanned using an nCounter Digital Analyzer to generate RCC files. Raw counts were normalized with the nSolver software (4.0) package using the geometric mean of both positive control probes and housekeeping probes. Lastly, logarithmic fold change, relative to the WT Chow group, was calculated using the normalized data obtained from nSolver.

Quantification of tissue and plasma metabolites and assessment of redox markers: Plasma and tissue metabolites were extracted and analyzed as described above (see Metabolite extraction, derivatization, and GC-MS analysis). Absolute quantification of metabolite pool sizes was performed by running calibration standards and normalizing GC-MS ion counts to the norvaline internal standard peak. Plasma and tissue pool sizes were expressed relative to plasma volume and tissue weight, respectively. For analysis of plasma and tissue ammonium concentration, 300 μL of sample extract was diluted with dH_2O to 1.5 mL and then analyzed using an Ammonia Gas Sensing Electrode (Thermo

Fisher Scientific, MA, USA) according to the user manual. Cytosolic and mitochondrial redox state for each tissue was estimated using enzymatic equilibrium relations described elsewhere^{36,97}. The cytosolic NADH/NAD⁺ was estimated from lactate dehydrogenase (LDH) equilibrium: $c\text{NADH}/\text{NAD}^+ = [\text{Lactate}]/[\text{Pyruvate}] \times K_{\text{LDH}}$; where $K_{\text{LDH}} = 1.11 \times 10^{-4}$. Similarly, a surrogate measure of cytosolic NADPH/NADP⁺ was estimated from the malate/pyruvate concentration ratio that is indicative of malic enzyme (ME) equilibrium. Lastly, mitochondrial NADH/NAD⁺ was estimated from glutamate dehydrogenase (GDH) equilibrium: $m\text{NADH}/\text{NAD}^+ = [\text{Glutamate}]/[\alpha\text{-ketoglutarate}][\text{NH}_4^+] \times K_{\text{GDH}}$; where $K_{\text{GDH}} = 3.87 \times 10^{-3} \text{ mM}$.

QUANTIFICATION AND STATISTICAL ANALYSIS

Unless otherwise specified, data are presented as means \pm SEM. Differences between groups were tested using ANOVA and Tukey multiple comparisons post hoc analysis. Analysis of histological scoring was performed using Kruskal-Wallis ANOVA with a Dunn's multiple comparisons test for post hoc analysis. Unless otherwise stated in figure legends, significant differences were defined as follows: *** $p < 0.01$, ** $p < 0.05$, and * $p < 0.1$.

Supplementary Material

Refer to Web version on PubMed Central for supplementary material.

ACKNOWLEDGMENTS

This research was supported by NIH grants R01 DK106348, U01 CA235508, and K01 DK135924, the Integrated Training in Engineering and Diabetes NIH training grant (T32 DK101003), the Vanderbilt Mouse Metabolic Phenotyping Center (NIH grants U24 DK059637 and S10 OD025199), the Vanderbilt Diabetes Research and Training Center (NIH grant P30 DK020593), the Vanderbilt Digestive Disease Research Center (NIH grant P30 DK058404), and the Vanderbilt-Ingram Cancer Center (NIH grant P30 CA068485). The graphical abstract and Figures 1, 2, 7, and S2 were prepared using BioRender. We thank Vanderbilt's Mouse Metabolic Phenotyping Center (MMPC) for assistance with the *in vivo* studies described here. We are also grateful to the Vanderbilt University Medical Center (VUMC) Analytical Services Core for the measurement of plasma insulin and cardiac free fatty acids. Additionally, we thank the VUMC Histology & Molecular Pathology Core for their assistance with the histological scoring of liver samples.

REFERENCES

- Burgess SC, He T, Yan Z, Lindner J, Sherry AD, Malloy CR, Browning JD, and Magnuson MA (2007). Cytosolic Phosphoenolpyruvate Carboxykinase Does Not Solely Control the Rate of Hepatic Gluconeogenesis in the Intact Mouse Liver. *Cell Metab.* 5, 313–320. 10.1016/j.cmet.2007.03.004. [PubMed: 17403375]
- Sauer U (2006). Metabolic networks in motion: 13C-based flux analysis. *Mol. Syst. Biol.* 2, 62. 10.1038/msb4100109. [PubMed: 17102807]
- Cheah YE, Hasenour CM, and Young JD (2017). In 13C Flux Analysis in Biotechnology and Medicine. In *Systems Biology* (John Wiley & Sons, Ltd), pp. 25–70. 10.1002/9783527696130.ch2.
- Kim I-Y, Park S, Kim Y, Chang Y, Choi CS, Suh S-H, and Wolfe RR (2020). In Vivo and In Vitro Quantification of Glucose Kinetics: From Bedside to Bench. *Endocrinol. Metab.* 35, 733–749. 10.3803/enm.2020.406.
- Bednarski TK, Rahim M, and Young JD (2021). In vivo 2H/13C flux analysis in metabolism research. *Curr. Opin. Biotechnol.* 71, 1–8. 10.1016/j.copbio.2021.04.005. [PubMed: 34048994]
- Song JD, Alves TC, Befroy DE, Perry RJ, Mason GF, Zhang XM, Munk A, Zhang Y, Zhang D, Cline GW, et al. (2020). Dissociation of Muscle Insulin Resistance from Alterations in

- Mitochondrial Substrate Preference. *Cell Metab.* 32, 726–735.e5. 10.1016/j.cmet.2020.09.008. [PubMed: 33035493]
7. Lewandowski ED (2023). Metabolic flux in the driver's seat during cardiac health and disease. *J. Mol. Cell. Cardiol* 182, 15–24. 10.1016/J.YJMCC.2023.07.004. [PubMed: 37451081]
 8. TeSlaa T, Bartman CR, Jankowski CSR, Zhang Z, Xu X, Xing X, Wang L, Lu W, Hui S, and Rabinowitz JD (2021). The Source of Glycolytic Intermediates in Mammalian Tissues. *Cell Metab.* 33, 367–378.e5. 10.1016/j.cmet.2020.12.020. [PubMed: 33472024]
 9. Axsom J, TeSlaa T, Lee WD, Chu Q, Cowan A, Bornstein MR, Neinast MD, Bartman CR, Blair MC, Li K, et al. (2024). Quantification of nutrient fluxes during acute exercise in mice. *Cell Metab.* 36, 2560–2579.e5. 10.1016/j.cmet.2024.09.010. [PubMed: 39413791]
 10. Hui S, Cowan AJ, Zeng X, Yang L, TeSlaa T, Li X, Bartman C, Zhang Z, Jang C, Wang L, et al. (2020). Quantitative Fluxomics of Circulating Metabolites. *Cell Metab.* 32, 676–688.e4. 10.1016/j.cmet.2020.07.013. [PubMed: 32791100]
 11. Wasserman DH (2009). Four Grams of Glucose at (American Physiological Society). 10.1152/ajpendo.90563.2008.
 12. Rahim M, Hasenour CM, Bednarski TK, Hughey CC, Wasserman DH, and Young JD (2021). Multitissue 2H/13C flux analysis reveals reciprocal upregulation of renal gluconeogenesis in hepatic PEPCK-C–knockout mice. *JCI Insight* 6, e149278. 10.1172/jci.insight.149278. [PubMed: 34156032]
 13. Farooqi IS, Yeo GS, Keogh JM, Aminian S, Jebb SA, Butler G, Cheetham T, and O'Rahilly S (2000). Dominant and recessive inheritance of morbid obesity associate with melanocortin 4 receptor deficiency. *J. Clin. Investig* 106, 271–279. 10.1172/JCI9397. [PubMed: 10903343]
 14. Loos RJF (2011). The genetic epidemiology of melanocortin 4 receptor variants. *Eur. J. Pharmacol* 660, 156–164. 10.1016/j.ej-phar.2011.01.033. [PubMed: 21295023]
 15. Itoh M, Suganami T, Nakagawa N, Tanaka M, Yamamoto Y, Kamei Y, Terai S, Sakaida I, and Ogawa Y (2011). Melanocortin 4 receptordeficient mice as a novel mouse model of nonalcoholic steatohepatitis. *Am. J. Pathol* 179, 2454–2463. 10.1016/j.ajpath.2011.07.014. [PubMed: 21906580]
 16. Hasenour CM, Kennedy AJ, Bednarski T, Trenary IA, Eudy BJ, da Silva RP, Boyd KL, and Young JD (2020). Vitamin E does not prevent Western diet-induced NASH progression and increases metabolic flux dysregulation in mice. *J. Lipid Res* 61, 707–721. 10.1194/jlr.RA119000183. [PubMed: 32086244]
 17. Itoh M, Kato H, Suganami T, Konuma K, Marumoto Y, Terai S, Sakugawa H, Kanai S, Hamaguchi M, Fukaishi T, et al. (2013). Hepatic Crown-Like Structure: A Unique Histological Feature in Non-Alcoholic Steatohepatitis in Mice and Humans. *PLoS One* 8, e82163. 10.1371/JOURNAL.PONE.0082163. [PubMed: 24349208]
 18. Sutton GM, Trevaskis JL, Hulver MW, McMillan RP, Markward NJ, Babin MJ, Meyer EA, and Butler AA (2006). Diet-Genotype Interactions in the Development of the Obese, Insulin-Resistant Phenotype of C57BL/6J Mice Lacking Melanocortin-3 or –4 Receptors. *Endocrinology* 147, 2183–2196. 10.1210/EN.2005-1209. [PubMed: 16469808]
 19. Young JD (2014). INCA: A computational platform for isotopically nonstationary metabolic flux analysis. *Bioinformatics* 30, 1333–1335. 10.1093/bioinformatics/btu015. [PubMed: 24413674]
 20. Hasenour CM, Wall ML, Ridley DE, Hughey CC, James FD, Wasserman DH, and Young JD (2015). Mass spectrometry-based microassay of 2H and 13C plasma glucose labelling to quantify liver metabolic fluxes in vivo. *Am. J. Physiol. Endocrinol. Metab* 309, E191–E203. 10.1152/ajpendo.00003.2015. [PubMed: 25991647]
 21. Hasenour CM, Ridley DE, James FD, Hughey CC, Donahue EP, Viollet B, Foretz M, Young JD, and Wasserman DH (2017). Liver AMP-Activated Protein Kinase Is Unnecessary for Gluconeogenesis but Protects Energy State during Nutrient Deprivation. *PLoS One* 12, e0170382. [PubMed: 28107516]
 22. Hughey CC, James FD, Bracy DP, Donahue EP, Young JD, Viollet B, Foretz M, and Wasserman DH (2017). Loss of hepatic AMP-activated protein kinase impedes the rate of glycogenolysis but not gluconeogenic fluxes in exercising mice. *J. Biol. Chem* 292, 20125–20140. 10.1074/jbc.M117.811547. [PubMed: 29038293]

23. Rome FI, Shobert GL, Voigt WC, Stagg DB, Puchalska P, Burgess SC, Crawford PA, and Hughey CC (2023). Loss of hepatic phosphoenolpyruvate carboxykinase 1 dysregulates metabolic responses to acute exercise but enhances adaptations to exercise training in mice. *Am. J. Physiol. Endocrinol. Metab* 324, E9–E23. 10.1152/ajpendo.00222.2022. [PubMed: 36351254]
24. Hasenour CM, Rahim M, and Young JD (2020). In Vivo Estimates of Liver Metabolic Flux Assessed by ¹³C-Propionate and ¹³C-Lactate Are Impacted by Tracer Recycling and Equilibrium Assumptions. *Cell Rep.* 32, 107986. 10.1016/j.celrep.2020.107986. [PubMed: 32755580]
25. Hasenour CM, Banerjee DR, and Young JD (2024). Metabolic Fluxes in the Renal Cortex Are Dysregulated In Vivo in Response to High-Fat Diet. *Diabetes* 73, 903–908. 10.2337/DB23-0710. [PubMed: 38502790]
26. Rahim M, Ragavan M, Deja S, Merritt ME, Burgess SC, and Young JD (2022). INCA 2.0: A tool for integrated, dynamic modeling of NMR- and MS-based isotopomer measurements and rigorous metabolic flux analysis. *Metab. Eng* 69, 275–285. 10.1016/j.ymben.2021.12.009. [PubMed: 34965470]
27. Hui S, Ghergurovich JM, Morscher RJ, Jang C, Teng X, Lu W, Esparza LA, Reya T, Le Zhan L, Yanxiang Guo J, et al. (2017). Glucose feeds the TCA cycle via circulating lactate. *Nature* 551, 115–118. 10.1038/nature24057. [PubMed: 29045397]
28. Faubert B, Li KY, Cai L, Hensley CT, Kim J, Zacharias LG, Yang C, Do QN, Doucette S, Burguete D, et al. (2017). Lactate Metabolism in Human Lung Tumors. *Cell* 171, 358–371.e9. 10.1016/j.cell.2017.09.019. [PubMed: 28985563]
29. Metallo CM, Walther JL, and Stephanopoulos G (2009). Evaluation of ¹³C isotopic tracers for metabolic flux analysis in mammalian cells. *J. Biotechnol* 144, 167–174. 10.1016/j.jbiotec.2009.07.010. [PubMed: 19622376]
30. Crown SB, Kelleher JK, Rouf R, Muoio DM, and Antoniewicz MR (2016). Comprehensive metabolic modeling of multiple ¹³C-isotopomer data sets to study metabolism in perfused working hearts. *Am. J. Physiol. Heart Circ. Physiol* 311, H881–H891. 10.1152/ajpheart.00428.2016. [PubMed: 27496880]
31. Malloy CR, Sherry AD, and Jeffrey FM (1990). Analysis of tricarboxylic acid cycle of the heart using ¹³C isotope isomers. *Am. J. Physiol* 259, H987–H995. 10.1152/ajpheart.1990.259.3.h987. [PubMed: 1975735]
32. Khairallah M, Labarthe F, Bouchard B, Danialou G, Petrof BJ, and Des Rosiers C (2004). Profiling substrate fluxes in the isolated working mouse heart using ¹³C-labeled substrates: focusing on the origin and fate of pyruvate and citrate carbons. *Am. J. Physiol. Circ. Physiol* 286, H1461–H1470. 10.1152/ajpheart.00942.2003.
33. Jensen J, Rustad PI, Kolnes AJ, and Lai YC (2011). The role of skeletal muscle glycogen breakdown for regulation of insulin sensitivity by exercise at Frontiers Media SA. *Front. Physiol* 2, 112. 10.3389/fphys.2011.00112. [PubMed: 22232606]
34. Satapati S, Kucejova B, Duarte JAG, Fletcher JA, Reynolds L, Sunny NE, He T, Nair LA, Livingston KA, Fu X, et al. (2015). Mitochondrial metabolism mediates oxidative stress and inflammation in fatty liver. *J. Clin. Investig* 125, 4447–4462. 10.1172/JCI82204. [PubMed: 26571396]
35. Sunny NE, Parks EJ, Browning JD, and Burgess SC (2011). Excessive hepatic mitochondrial TCA cycle and gluconeogenesis in humans with nonalcoholic fatty liver disease. *Cell Metab.* 14, 804–810. 10.1016/j.cmet.2011.11.004. [PubMed: 22152305]
36. Cappel DA, Deja S, Duarte JAG, Kucejova B, Iñigo M, Fletcher JA, Fu X, Berglund ED, Liu T, Elmquist JK, et al. (2019). Pyruvate-Carboxylase-Mediated Anaplerosis Promotes Antioxidant Capacity by Sustaining TCA Cycle and Redox Metabolism in Liver. *Cell Metab.* 29, 1291–1305.e8. 10.1016/j.cmet.2019.03.014. [PubMed: 31006591]
37. Fisher-Wellman KH, and Neuffer PD (2012). Linking mitochondrial bioenergetics to insulin resistance via redox biology. *Trends Endocrinol. Metab* 23, 142–153. 10.1016/j.tem.2011.12.008. [PubMed: 22305519]
38. Hausler N, Browning J, Merritt M, Storey C, Milde A, Jeffrey FMH, Sherry AD, Malloy CR, and Burgess SC (2006). Effects of insulin and cytosolic redox state on glucose production pathways in the isolated perfused mouse liver measured by integrated ²H and ¹³C NMR. *Biochem. J* 394, 465–473. 10.1042/BJ20051174. [PubMed: 16288601]

39. Kobayashi K, and Neely JR (1979). Control of Maximum Rates of Glycolysis in Rat Cardiac Muscle. *Circ. Res* 44, 166–175. [PubMed: 216503]
40. Qi Y, Xu Z, Zhu Q, Thomas C, Kumar R, Feng H, Dostal DE, White MF, Baker KM, and Guo S (2013). Myocardial loss of IRS1 and IRS2 causes heart failure and is controlled by p38a MAPK during insulin resistance. *Diabetes* 62, 3887–3900. 10.2337/db13-0095. [PubMed: 24159000]
41. Zhang S, Hulver MW, McMillan RP, Cline MA, and Gilbert ER (2014). The pivotal role of pyruvate dehydrogenase kinases in metabolic flexibility. *Nutr. Metab* 111, 10.1186/1743-7075-11-10.
42. Seiler SE, Martin OJ, Noland RC, Slentz DH, DeBalsi KL, Ilkayeva OR, An J, Newgard CB, Koves TR, and Muoio DM (2014). Obesity and lipid stress inhibit carnitine acetyltransferase activity. *J. Lipid Res* 55, 635–644. 10.1194/jlr.M043448. [PubMed: 24395925]
43. Liang X, Liu L, Fu T, Zhou Q, Zhou D, Xiao L, Liu J, Kong Y, Xie H, Yi F, et al. (2016). Exercise Inducible Lactate Dehydrogenase B Regulates Mitochondrial Function in Skeletal Muscle. *J. Biol. Chem* 291, 25306–25318. 10.1074/jbc.M116.749424. [PubMed: 27738103]
44. Perry RJ, Peng L, Cline GW, Butrico GM, Wang Y, Zhang XM, Rothman DL, Petersen KF, and Shulman GI (2017). Non-invasive assessment of hepatic mitochondrial metabolism by positional isotopomer NMR tracer analysis (PINTA). *Nat. Commun* 8, 798. 10.1038/s41467-017-01143-w. [PubMed: 28986525]
45. Korac B, Kalezic A, Pekovic-Vaughan V, Korac A, and Jankovic A (2021). Redox changes in obesity, metabolic syndrome, and diabetes. *Redox Biol.* 42, 101887. 10.1016/j.redox.2021.101887. [PubMed: 33579666]
46. Luukkonen PK, Qadri S, Ahlholm N, Porthan K, Männistö V, Sammalkorpi H, Penttilä AK, Hakkarainen A, Lehtimäki TE, Gaggini M, et al. (2022). Distinct contributions of metabolic dysfunction and genetic risk factors in the pathogenesis of non-alcoholic fatty liver disease. *J. Hepatol* 76, 526–535. 10.1016/j.jhep.2021.10.013. [PubMed: 34710482]
47. Grundler ML, Smith SL, and Preves DM (1989). The effect of diet on multiple site regulation of glycolysis in rat skeletal muscle. 1. Glucose metabolism and intracellular metabolites. *Nutr. Res* 9, 735–749. 10.1016/S0271-5317(89)80017-X.
48. Seyssel K, Alligier M, Meugnier E, Chanseaux E, Loizon E, Canto C, Disse E, Lambert-Porcheron S, Brozek J, Blond E, et al. (2014). Regulation of energy metabolism and mitochondrial function in skeletal muscle during lipid overfeeding in healthy men. *J. Clin. Endocrinol. Metab* 99, 1254–1262. 10.1210/jc.2013-4379.
49. Utriainen T, Takala T, Luotolahti M, Rönnemaa T, Laine H, Ruotsalainen U, Haaparanta M, Nuutila P, and Yki-Järvinen H (1998). Insulin resistance characterizes glucose uptake in skeletal muscle but not in the heart in NIDDM. *Diabetologia* 41, 555–559. 10.1007/s001250050946. [PubMed: 9628273]
50. Nuutila P, Knuuti J, Ruotsalainen U, Koivisto VA, Eronen E, Teräs M, Bergman J, Haaparanta M, Voipio-Pulkki LM, Viikari J, et al. (1993). Insulin resistance is localized to skeletal but not heart muscle in type 1 diabetes. *Am. J. Physiol* 264, E756–E762. 10.1152/ajpendo.1993.264.5.e756. [PubMed: 8498497]
51. Vom Dahl J, Herman WH, Hicks RJ, Ortiz-Alonso FJ, Lee KS, Allman KC, Wolfe ER, Kalff V, and Schwaiger M (1993). Myocardial glucose uptake in patients with insulin-dependent diabetes mellitus assessed quantitatively by dynamic positron emission tomography. *Circulation* 88, 395–404. 10.1161/01.CIR.88.2.395. [PubMed: 8339403]
52. Ussher JR, Koves TR, Jaswal JS, Zhang L, Ilkayeva O, Dyck JRB, Muoio DM, and Lopaschuk GD (2009). Insulin-stimulated cardiac glucose oxidation is increased in high-fat diet-induced obese mice lacking malonyl CoA decarboxylase. *Diabetes* 58, 1766–1775. 10.2337/db09-0011. [PubMed: 19478144]
53. Buchanan J, Mazumder PK, Hu P, Chakrabarti G, Roberts MW, Yun UJ, Cooksey RC, Litwin SE, and Abel ED (2005). Reduced cardiac efficiency and altered substrate metabolism precedes the onset of hyperglycemia and contractile dysfunction in two mouse models of insulin resistance and obesity. *Endocrinology* 146, 5341–5349. 10.1210/en.2005-0938. [PubMed: 16141388]
54. Ussher JR, and Lopaschuk GD (2013). Cardiac insulin resistance: It's sweeter than you think. *Endocrinology* 154, 2575–2578. 10.1210/en.2013-1506. [PubMed: 23873770]

55. Gupte AA, Minze LJ, Reyes M, Ren Y, Wang X, Brunner G, Ghosn M, Cordero-Reyes AM, Ding K, Pratico D, et al. (2013). High-fat feeding-induced hyperinsulinemia increases cardiac glucose uptake and mitochondrial function despite peripheral insulin resistance. *Endocrinology* 154, 2650–2662. 10.1210/en.2012-2272. [PubMed: 23709089]
56. Ritterhoff J, Young S, Villet O, Shao D, Neto FC, Bettcher LF, Hsu Y-WA, Kolwicz SC, Raftery D, and Tian R (2020). Metabolic Remodeling Promotes Cardiac Hypertrophy by Directing Glucose to Aspartate Biosynthesis. *Circ. Res* 126, 182–196. 10.1161/CIRCRESAHA.119.315483. [PubMed: 31709908]
57. Taegtmeier H, and Overturf ML (1988). Effects of moderate hypertension on cardiac function and metabolism in the rabbit. *Hypertension* 11, 416–426. 10.1161/01.HYP.11.5.416. [PubMed: 3366475]
58. Befroy DE, Petersen KF, Dufour S, Mason GF, de Graaf RA, Rothman DL, and Shulman GI (2007). Impaired Mitochondrial Substrate Oxidation in Muscle of Insulin-Resistant Offspring of Type 2 Diabetic Patients. *Diabetes* 56, 1376–1381. 10.2337/db06-0783. [PubMed: 17287462]
59. De Feyter HM, Lenaers E, Houten SM, Schrauwen P, Hesselink MK, Wanders RJA, Nicolay K, and Prompers JJ (2008). Increased intramyocellular lipid content but normal skeletal muscle mitochondrial oxidative capacity throughout the pathogenesis of type 2 diabetes. *FASEB J.* 22, 3947–3955. 10.1096/fj.08-112318. [PubMed: 18653763]
60. Hancock CR, Han DH, Chen M, Terada S, Yasuda T, Wright DC, and Holloszy JO (2008). High-fat diets cause insulin resistance despite an increase in muscle mitochondria. *Proc. Natl. Acad. Sci. USA* 105, 7815–7820. 10.1073/pnas.0802057105. [PubMed: 18509063]
61. Damsbo P, Vaag A, Hother-Nielsen O, and Beck-Nielsen H (1991). Reduced glycogen synthase activity in skeletal muscle from obese patients with and without Type 2 (non-insulin-dependent) diabetes mellitus. *Diabetologia* 34, 239–245. 10.1007/BF00405082. [PubMed: 1906024]
62. Pedersen SB, Børglum JD, Schmitz O, Bak JF, Sørensen NS, and Richelsen B (1993). Abdominal obesity is associated with insulin resistance and reduced glycogen synthase activity in skeletal muscle. *Metabolism* 42, 998–1005. 10.1016/0026-0495(93)90013-E. [PubMed: 8345824]
63. Sugden MC, and Holness MJ (2006). Mechanisms underlying regulation of the expression and activities of the mammalian pyruvate dehydrogenase kinases. *Arch. Physiol. Biochem* 112, 139–149. 10.1080/13813450600935263. [PubMed: 17132539]
64. Gavin TP, Ernst JM, Kwak HB, Caudill SE, Reed MA, Garner RT, Nie Y, Weiss JA, Pories WJ, Dar M, et al. (2018). High incomplete skeletal muscle fatty acid oxidation explains low muscle insulin sensitivity in poorly controlled T2D. *J. Clin. Endocrinol. Metab* 103, 882–889. 10.1210/jc.2017-01727. [PubMed: 29155999]
65. Baker PR, Boyle KE, Koves TR, Ilkayeva OR, Muoio DM, Houmard JA, and Friedman JE (2015). Metabolomic analysis reveals altered skeletal muscle amino acid and fatty acid handling in obese humans. *Obesity* 23, 981–988. 10.1002/oby.21046. [PubMed: 25864501]
66. Koves TR, Ussher JR, Noland RC, Slentz D, Mosedale M, Ilkayeva O, Bain J, Stevens R, Dyck JRB, Newgard CB, et al. (2008). Mitochondrial Overload and Incomplete Fatty Acid Oxidation Contribute to Skeletal Muscle Insulin Resistance. *Cell Metab.* 7, 45–56. 10.1016/J.CMET.2007.10.013. [PubMed: 18177724]
67. Kelley DE (2005). Skeletal muscle fat oxidation: timing and flexibility are everything. *J. Clin. Investig* 115, 1699–1702. 10.1172/JCI25758. [PubMed: 16007246]
68. Green HJ, Daub B, Houston ME, Thomson JA, Fraser I, and Ranney D (1981). Human vastus lateralis and gastrocnemius muscles. A comparative histochemical and biochemical analysis. *J. Neurol. Sci* 52, 201–210. 10.1016/0022-510X(81)90005-8. [PubMed: 6171618]
69. Wade AJ, Marbut MM, and Round JM (1990). Muscle fibre type and aetiology of obesity. *Lancet* 335, 805–808. 10.1016/0140-6736(90)90933-V. [PubMed: 1969558]
70. Hickey MS, Carey JO, Azevedo JL, Houmard JA, Pories WJ, Israel RG, and Dohm GL (1995). Skeletal muscle fiber composition is related to adiposity and in vitro glucose transport rate in humans. *Am. J. Physiol* 268, E453–E457. 10.1152/ajpendo.1995.268.3.E453268. [PubMed: 7900793]

71. Serrano N, Hyatt JPK, Houmard JA, Murgia M, and Katsanos CS (2023). Muscle fiber phenotype: a culprit of abnormal metabolism and function in skeletal muscle of humans with obesity. *Am. J. Physiol. Endocrinol. Metab* 325, E723–E733. 10.1152/ajpendo.00190.2023. [PubMed: 37877797]
72. Patterson RE, Kalavalapalli S, Williams CM, Nautiyal M, Mathew JT, Martinez J, Reinhard MK, McDougall DJ, Rocca JR, Yost RA, et al. (2016). Lipotoxicity in steatohepatitis occurs despite an increase in tricarboxylic acid cycle activity. *Am. J. Physiol. Endocrinol. Metab* 310, E484–E494. 10.1152/ajpendo.00492.2015. [PubMed: 26814015]
73. Maurya SK, Carley AN, Maurya CK, and Lewandowski ED (2023). Western Diet Causes Heart Failure With Reduced Ejection Fraction and Metabolic Shifts After Diastolic Dysfunction and Novel Cardiac Lipid Derangements. *JACC Basic Transl. Sci* 8, 422–435. 10.1016/J.JACBTS.2022.10.009. [PubMed: 37138801]
74. Cuendet GS, Loten EG, Jeanrenaud B, and Renold AE (1976). Decreased basal, noninsulin stimulated glucose uptake and metabolism by skeletal soleus muscle isolated from obese hyperglycemic (ob/ob) mice. *J. Clin. Investig* 58, 1078–1088. 10.1172/JCI108559. [PubMed: 993331]
75. Sparks LM, Xie H, Koza RA, Mynatt R, Hulver MW, Bray GA, and Smith SR (2005). A high-fat diet coordinately downregulates genes required for mitochondrial oxidative phosphorylation in skeletal muscle. *Diabetes* 54, 1926–1933. [PubMed: 15983191]
76. Liu S, Dai Z, Cooper DE, Kirsch DG, and Locasale JW (2020). Quantitative Analysis of the Physiological Contributions of Glucose to the TCA Cycle. *Cell Metab.* 32, 619–628.e21. 10.1016/j.cmet.2020.09.005. [PubMed: 32961109]
77. Zimmer HG (1992). The oxidative pentose phosphate pathway in the heart: Regulation, physiologic significance, and clinical implications. *Basic Res. Cardiol* 87, 303–316. 10.1007/BF00796517.
78. Glock GE, and McLean P (1954). Levels of enzymes of the direct oxidative pathway of carbohydrate metabolism in mammalian tissues and tumours. *Biochem. J* 56, 171–175. 10.1042/bj0560171. [PubMed: 13126112]
79. McCloskey D, Young JD, Xu S, Palsson BO, and Feist AM (2016). MID Max: LC-MS/MS Method for Measuring the Precursor and Product Mass Isotopomer Distributions of Metabolic Intermediates and Cofactors for Metabolic Flux Analysis Applications. *Anal. Chem* 88, 1362–1370. 10.1021/acs.analchem.5b03887. [PubMed: 26666286]
80. Hubbard BT, LaMoia TE, Goedeke L, Gaspar RC, Galsgaard KD, Kahn M, Mason GF, and Shulman GI (2023). Q-Flux: A method to assess hepatic mitochondrial succinate dehydrogenase, methylmalonyl-CoA mutase, and glutaminase fluxes in vivo. *Cell Metab.* 35, 212–226.e4. 10.1016/J.CMET.2022.11.011. [PubMed: 36516861]
81. Satapati S, Sunny NE, Kucejova B, Fu X, He TT, Méndez-Lucas A, Shelton JM, Perales JC, Browning JD, and Burgess SC (2012). Elevated TCA cycle function in the pathology of diet-induced hepatic insulin resistance and fatty liver. *J. Lipid Res* 53, 1080–1092. 10.1194/jlr.M023382. [PubMed: 22493093]
82. Litt MJ, Okoye GD, Lark D, Cakir I, Moore C, Barber MC, Atkinson J, Fessel J, Moslehi J, and Cone RD (2017). Loss of the melanocortin-4 receptor in mice causes dilated cardiomyopathy. *Elife* 6, e28118–e28121. 10.7554/eLife.28118. [PubMed: 28829041]
83. Jenkins AB, Furler SM, and Kraegen EW (1986). 2-deoxy-d-glucose metabolism in individual tissues of the rat in vivo. *Int. J. Biochem* 18, 311–318. 10.1016/0020-711X(86)90036-4. [PubMed: 3519306]
84. Ayala JE, Bracy DP, McGuinness OP, and Wasserman DH (2006). Considerations in the design of hyperinsulinemic-euglycemic clamps in the conscious mouse. *Diabetes* 55, 390–397. 10.2337/dia-betes.55.02.06.db05-0686. [PubMed: 16443772]
85. Lee WD, Liang L, AbuSalim J, Jankowski CSR, Samarah LZ, Neinast MD, and Rabinowitz JD (2023). Impact of acute stress on murine metabolomics and metabolic flux. *Proc. Natl. Acad. Sci* 120, e2301215120. 10.1073/pnas.2301215120. [PubMed: 37186827]
86. Fedorov A, Lehto A, and Klein J (2023). Inhibition of mitochondrial respiration by general anesthetic drugs. *Naunyn-Schmiedeberg Arch Pharmacol* 396, 375–381. 10.1007/s00210-022-02338-9. [PubMed: 36385685]

87. Neinast MD, Jang C, Hui S, Murashige DS, Chu Q, Morscher RJ, Li X, Zhan L, White E, Anthony TG, et al. (2019). Quantitative Analysis of the Whole-Body Metabolic Fate of Branched-Chain Amino Acids. *Cell Metab.* 29, 417–429.e4. 10.1016/J.CMET.2018.10.013/ATTACHMENT/09003D63-E71A-4EB7-A8D7-9041C172B553/MMC3.PDF. [PubMed: 30449684]
88. Brooks SPJ, Lampi BJ, and Bihun CG (1999). The Influence of Euthanasia Methods on Rat Liver Metabolism. *Contemp. Top. Lab. Anim. Sci* 38, 19–24. [PubMed: 12086442]
89. Overmyer KA, Thonusin C, Qi NR, Burant CF, and Evans CR (2015). Impact of anesthesia and euthanasia on metabolomics of mammalian tissues: Studies in a C57BL/6J mouse model. *PLoS One* 10, e0117232. 10.1371/journal.pone.0117232. [PubMed: 25658945]
90. Gan Z, Fu Z, Stowe JC, Powell FL, and McCulloch AD (2016). A protocol to collect specific mouse skeletal muscles for metabolomics studies. *Methods Mol. Biol* 1375, 169–179. 10.1007/7651_2015_248. [PubMed: 26003134]
91. Huszar D, Lynch CA, Fairchild-Huntress V, Dunmore JH, Fang Q, Berkemeier LR, Gu W, Kesterson RA, Boston BA, Cone RD, et al. (1997). Targeted disruption of the melanocortin-4 receptor results in obesity in mice. *Cell* 88, 131–141. 10.1016/S0092-8674(00)81865-6. [PubMed: 9019399]
92. Bedossa P, FLIP Pathology Consortium, Gouw AHA, Lackner C, Schirmacher P, Terracciano L, Tiniakos D, Brain J, Bury Y, Cabibi D, et al. (2014). Utility and appropriateness of the fatty liver inhibition of progression (FLIP) algorithm and steatosis, activity, and fibrosis (SAF) score in the evaluation of biopsies of nonalcoholic fatty liver disease. *Hepatology* 60, 565–575. 10.1002/hep.27173. [PubMed: 24753132]
93. Young JD, Allen DK, and Morgan JA (2014). Isotopomer measurement techniques in metabolic flux analysis II: Mass spectrometry. *Methods Mol. Biol* 1083, 85–108. 10.1007/978-1-62703-661-0_7. [PubMed: 24218212]
94. Gomez JD, Wall ML, Rahim M, Kambhampati S, Evans BS, Allen DK, Antoniewicz MR, and Young JD (2023). Program for Integration and Rapid Analysis of Mass Isotopomer Distributions (PIRAMID). *Bioinformatics* 39, btad661. 10.1093/bioinformatics/btad661. [PubMed: 37889279]
95. Steele R. (1959). Influences of glucose loading and or injected insulin on hepatic glucose output. *Ann. N. Y. Acad. Sci* 82, 420–430. 10.1111/j.1749-6632.1959.tb44923.x. [PubMed: 13833973]
96. Kraegen EW, James DE, Jenkins AB, and Chisholm DJ (1985). Dose-response curves for in vivo insulin sensitivity in individual tissues in rats. *Am. J. Physiol* 248, E353–E362. 10.1152/ajpendo.1985.248.3.E353. [PubMed: 3883806]
97. Krebs HA, and Veech RL (1969). Equilibrium relations between pyridine nucleotides and adenine nucleotides and their roles in the regulation of metabolic processes. *Adv. Enzyme Regul* 7, 397–413. 10.1016/0065-2571(69)90030-2. [PubMed: 4391643]

Highlights

- Multi-organ MFA quantifies fluxes in liver, heart, and muscle *in vivo*
- Obesity increases hepatic gluconeogenesis and cardiac glucose oxidation
- Skeletal muscle fluxes decline, indicative of metabolic inflexibility in obesity
- Multi-tissue MFA provides a scalable platform for assessing tissue-specific fluxes

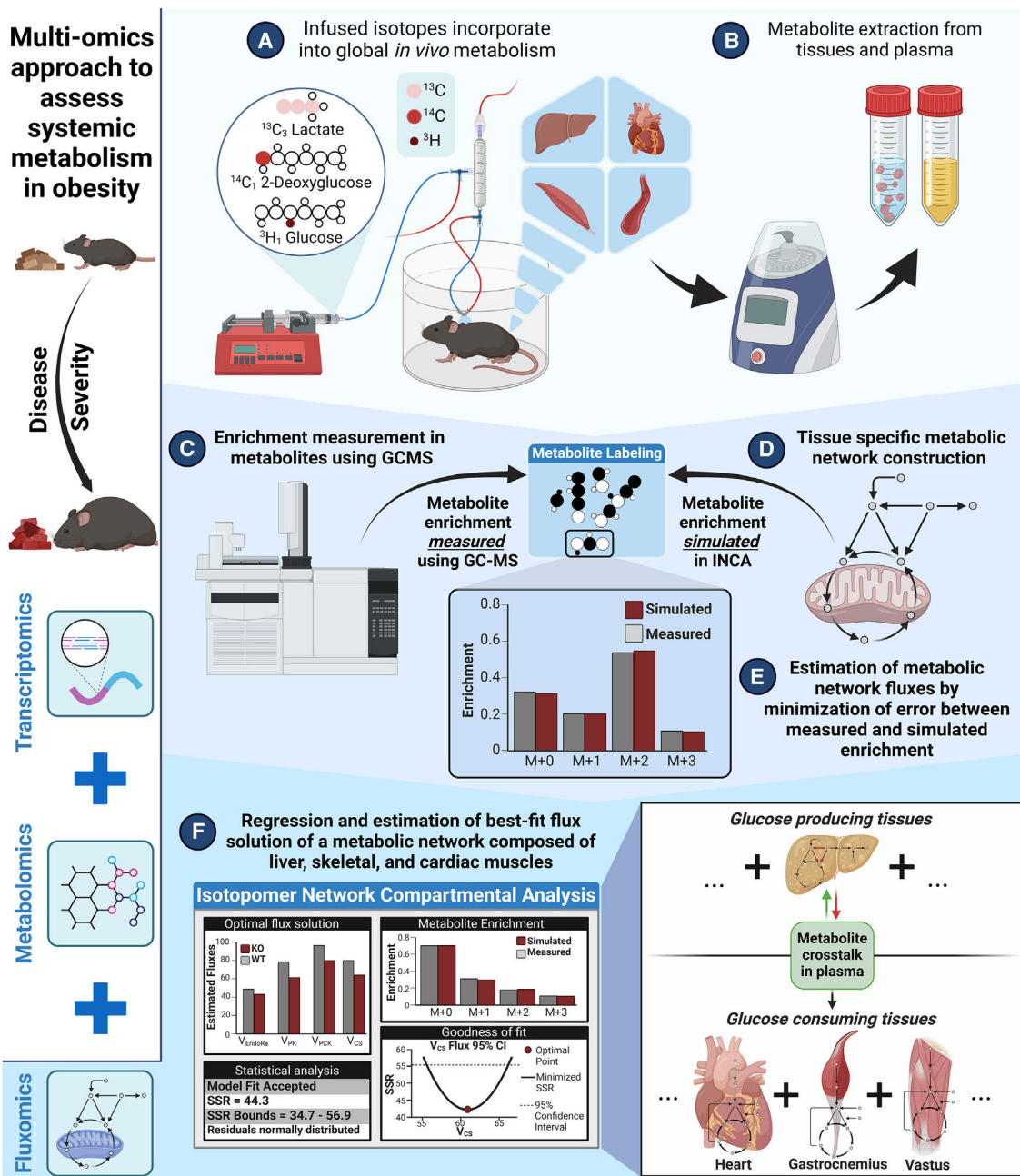


Figure 1. Overview of study design and fluxomics approach
 The steps (A–F) involved in multi-tissue MFA are highlighted.

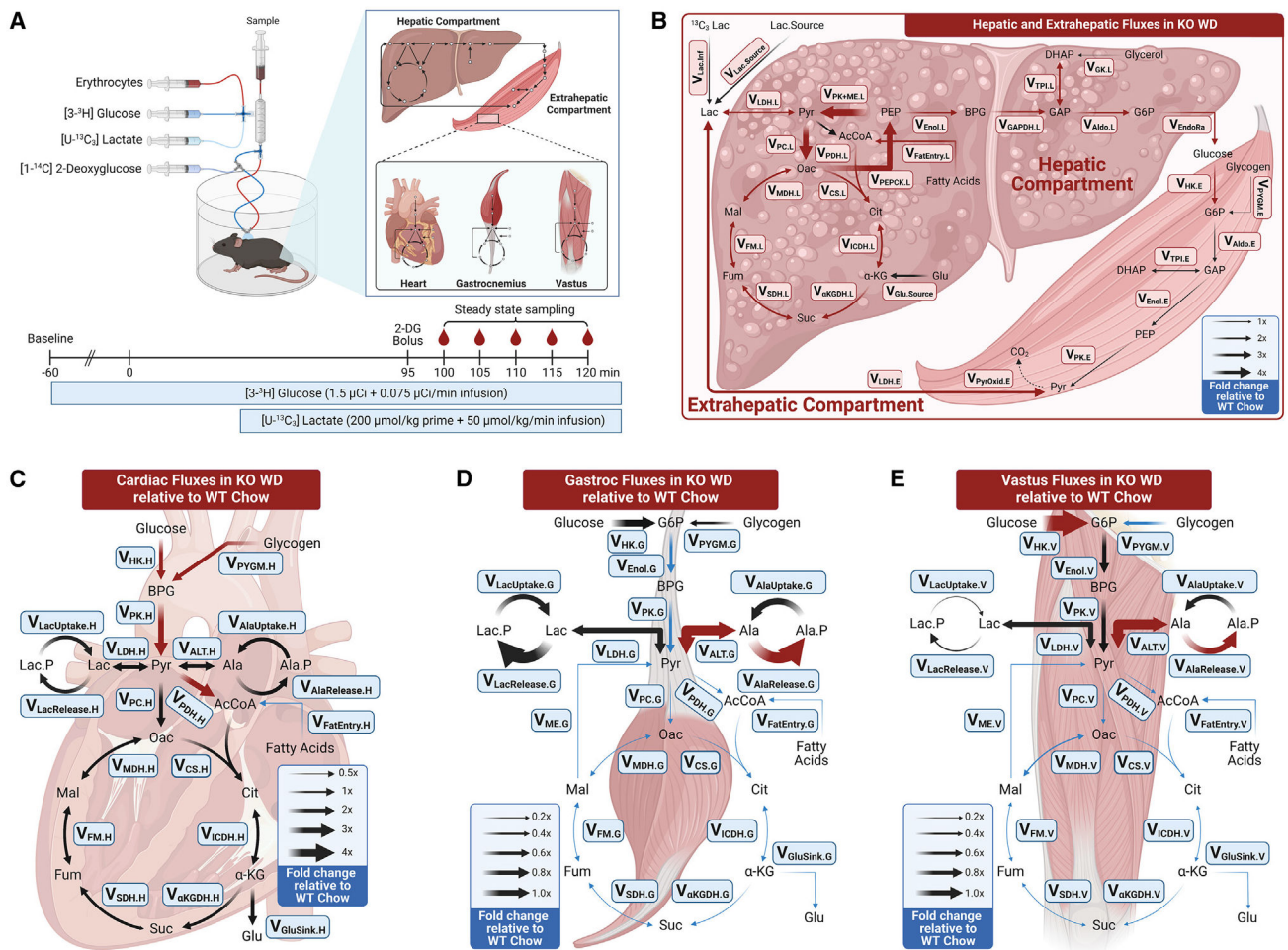


Figure 2. Multi-organ assessment of metabolic fluxes in genetically obese, Western-diet-fed mice reveals discordant effects in liver, heart, and skeletal muscle

(A) Overview of isotope infusion protocol. Fold change in absolute fluxes assessed in the (B) liver, (C) heart, (D) gastrocnemius, and (E) vastus tissues of KO WD ($n = 6$) mice relative to WT chow ($n = 8$) controls. The map represents the metabolic network shown in Table S2. Red and blue arrows represent fluxes that are significantly increased or decreased in KO WD mice compared to WT chow mice, respectively ($p < 0.05$).

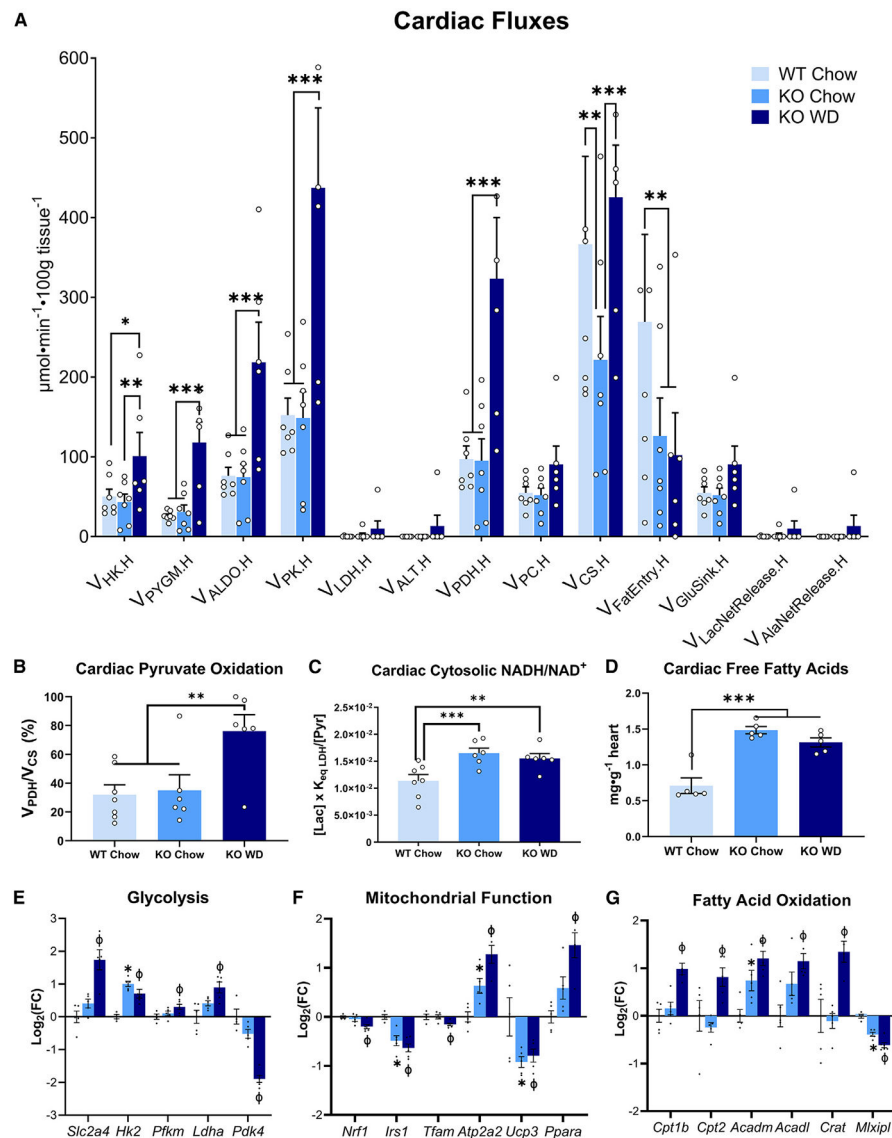


Figure 4. Myocardial glucose and fatty acid oxidation are reciprocally altered by hyperphagic Western diet feeding

(A) Absolute metabolic fluxes, (B) pyruvate oxidation relative to V_{CS} , (C) cytosolic redox state, and (D) free fatty acids in the hearts of WT chow ($n = 8$), KO chow ($n = 7$), and KO WD mice ($n = 6$) (* $p < 0.10$, ** $p < 0.05$, and *** $p < 0.01$). Gene expression of proteins that regulate (E) glycolysis, (F) mitochondrial function, and (G) fat oxidation in the heart (* $p < 0.05$ for WT chow vs. KO chow and $\Phi p < 0.05$ for WT chow vs. KO WD). Data are represented as the mean \pm SEM.

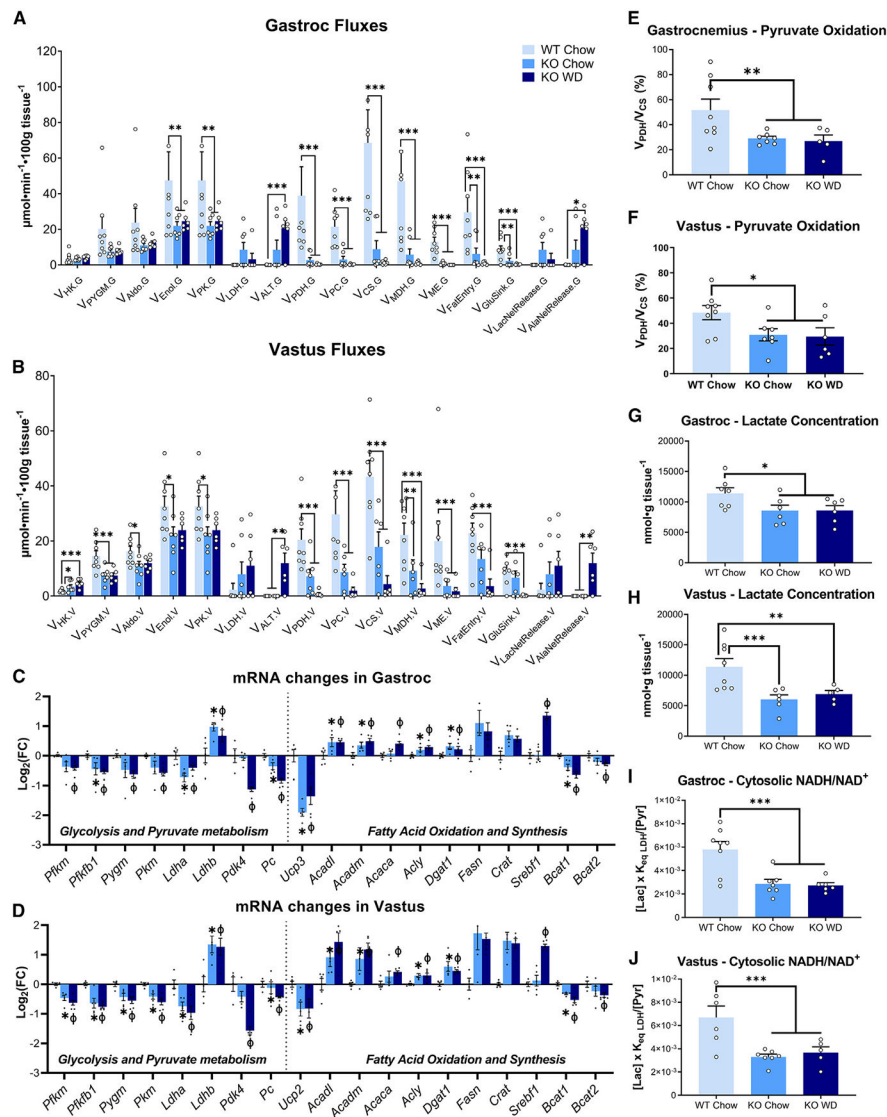


Figure 5. Obese mice have reduced glycolytic and mitochondrial oxidative fluxes in skeletal muscle

(A–D) Absolute fluxes estimated in the (A) gastrocnemius and (B) vastus skeletal muscles of WT chow ($n = 8$), KO chow ($n = 7$), and KO WD mice ($n = 6$) (* $p < 0.10$, ** $p < 0.05$, and *** $p < 0.01$). Log fold change in gene expression of proteins regulating glycolysis, pyruvate metabolism, and fatty acid metabolism in (C) gastrocnemius and (D) vastus muscles (* $p < 0.05$ for WT chow vs. KO chow and $\Phi p < 0.05$ for WT chow vs. KO WD).

(E and F) Pyruvate oxidation relative to V_{CS} .

(G–J) (G and H) Lactate concentration and (I and J) cytosolic NADH:NAD⁺ ratio, assessed using metabolite concentration, in the gastrocnemius and vastus tissues (* $p < 0.10$, ** $p < 0.05$, and *** $p < 0.01$).

Data are represented as the mean \pm SEM.

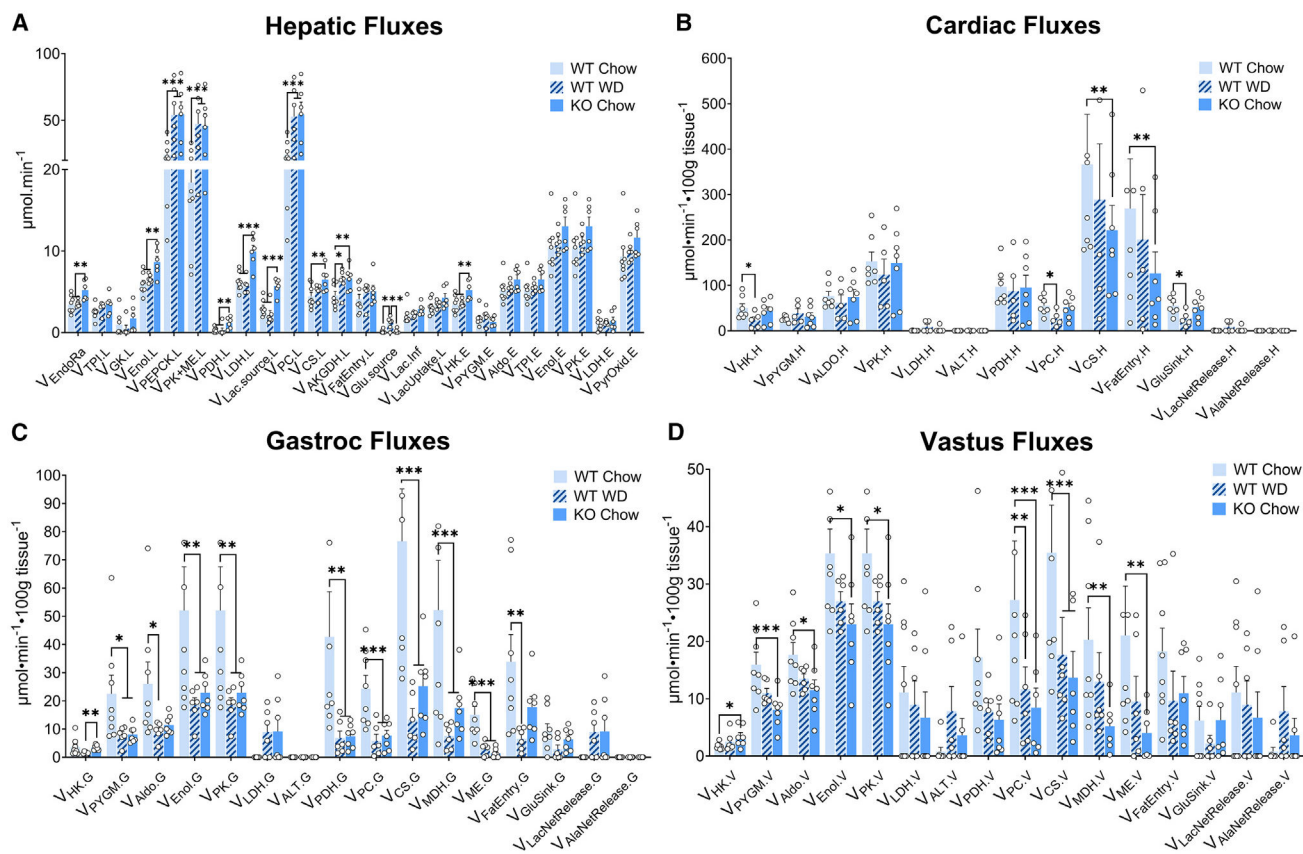


Figure 6. Moderate obesity caused by Western diet feeding of wild-type mice leads to similar changes in metabolic fluxes compared with those observed in chow-fed hyperphagic mice
 Absolute fluxes estimated in the (A) liver, (B) heart, (C) gastrocnemius, and (D) vastus skeletal muscle of WT chow ($n = 8$), WTWD ($n = 6$), and KO chow ($n = 7$) mice (* $p < 0.10$, ** $p < 0.05$, and *** $p < 0.01$). Data are represented as the mean \pm SEM.

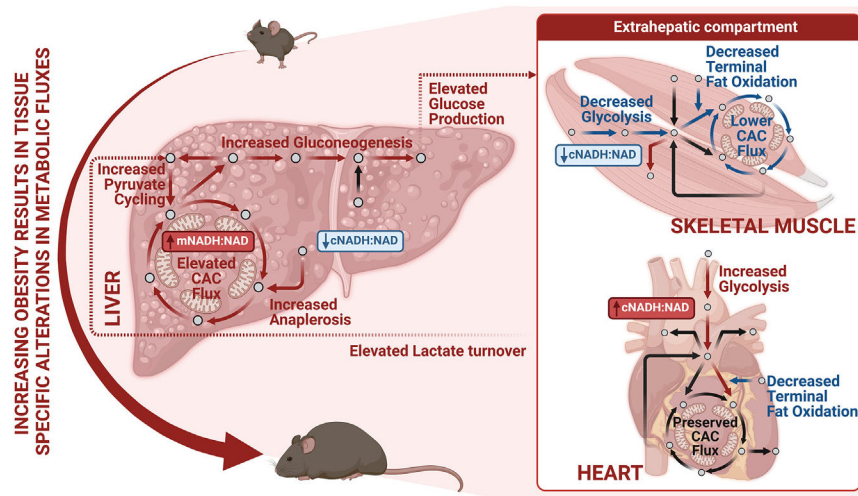


Figure 7. Overview of major metabolic changes in the liver, skeletal muscle, and heart of obese mice

Livers of obese mice exhibited increased oxidative and gluconeogenic fluxes. Heart muscle and skeletal muscle exhibited opposite changes in energy metabolism and cytosolic redox state.

KEY RESOURCES TABLE

REAGENT or RESOURCE	SOURCE	IDENTIFIER
Chemicals, peptides, and recombinant proteins		
Methoxamine (MOX) Reagent	Thermo Fisher Scientific	Cat. No: TS-45950
MTBSTFA + 1% TBDMCS Silylation Reagent	Thermo Fisher Scientific	Cat. No: TS-48927
Sodium L-Lactate (¹³ C ₃ , 98%) 20% W/W in H ₂ O	Cambridge Isotope Laboratories	Cat. No: CLM-1579-MPT-PK
[1- ¹⁴ C]2-Deoxy-D-Glucose	Revvity	Cat. No: NEC495A
D-[3- ³ H]-Glucose	Revvity	Cat. No: NET331C
Methanol	Sigma Aldrich	Cat. No: 1008372500
Chloroform	Sigma Aldrich	Cat. No: 1024322500
Water	Sigma Aldrich	Cat. No: 1037022500
TRIzol™ Reagent	Invitrogen	Cat. No: 15596026
Critical commercial assays		
nCounter mRNA Custom CodeSet	NanoString	Cat No: 116000001
RNeasy Mini Kit	Qiagen	Cat. No: 74104
Deposited data		
Absolute flux measurements	This Paper	Mendeley Data: https://dx.doi.org/10.17632/dxc5yxysnm.1
Mass isotopomer distribution (MID) data	This Paper	Mendeley Data: https://dx.doi.org/10.17632/dxc5yxysnm.1
Metabolite concentrations	This Paper	Mendeley Data: https://dx.doi.org/10.17632/dxc5yxysnm.1
mRNA fold change data	This Paper	Mendeley Data: https://dx.doi.org/10.17632/dxc5yxysnm.1
NanoString nCounter raw RCC files	This paper	GEO accession number GSE291838
Experimental models: Organisms/strains		
Mouse: <i>Mc4r</i> ^{-/-} (C57Bl/6J)	Huszar et al. (1997)	https://doi.org/10.1016/S0092-8674(00)81865-6
Software and algorithms		
BioRender	BioRender	https://www.biorender.com/
Isotopomer Network Compartmental Analysis (INCA 2.0)	Rahim et al. (2022)	https://doi.org/10.1016/j.ymben.2021.12.009 https://mfa.vueinnovations.com/
MATLAB 2024a	Mathworks	https://www.mathworks.com/
Microsoft Office 365	Microsoft	https://www.microsoft.com/en-us/microsoft-365/microsoft-365-education
nSolver	NanoString	https://nanosttring.com
Prism 9	GraphPad	https://www.graphpad.com/